Widespread epistasis shapes RNA Polymerase II active site function and evolution

Authors: Bingbing Duan[1], Chenxi Qiu[2], Sing-Hoi Sze[3, 4], Craig Kaplan[1*]

Affiliations:

[1] Department of Biological Sciences, University of Pittsburgh, Pittsburgh, PA 15260, USA

[2] Department of Genetics, Harvard Medical School, Boston, MA 02215, USA

[3] Department of Computer Science and Engineering, Texas A&M University, College Station, TX 77843, USA

[4] Department of Biochemistry & Biophysics, Texas A&M University, College Station, TX 77843, USA

Contact information: craig.kaplan@pitt.edu

ABSTRACT

Multi-subunit RNA Polymerases (msRNAPs) are responsible for transcription in all kingdoms of life. These enzymes rely on dynamic, highly conserved active site domains such as the so-called “trigger loop” (TL) to accomplish steps in the transcription cycle. Mutations in the RNA polymerase II (Pol II) TL confer a spectrum of biochemical and genetic phenotypes that suggest two main classes, which decrease or increase catalysis or other nucleotide addition cycle (NAC) events. The Pol II active site relies on networks of residue interactions to function and mutations likely perturb these networks in ways that may alter mechanisms. We have undertaken a structural genetics approach to reveal residue interactions within and surrounding the Pol II TL – determining its “interaction landscape” – by deep mutational scanning in *Saccharomyces cerevisiae* Pol II. This analysis reveals connections between TL residues and surrounding domains, demonstrating that TL function is tightly coupled to its specific enzyme context.

INTRODUCTION

Transcription from cellular genomes is performed by conserved multi-subunit RNA polymerases (msRNAPs)[1-3]. While bacteria and archaea use a single msRNAP to transcribe all RNAs[4-6], eukaryotes have at least three msRNAPs (Pol I, II, and III) for different RNA types[7-10]. RNA synthesis by msRNAPs occurs by iterative nucleotide addition cycles (NAC) of nucleotide selection, catalysis and polymerase translocation[11-15]. The msRNAPs active sites accomplish these NAC steps using two conformationally flexible domains, the bridge helix (BH) and trigger loop (TL)[5,12,16-19]. The multi-functional natures of the BH and TL likely underlie their striking conservation, serving as interesting models for studying the function and evolution of extremely constrained protein domains.

Most catalytic cycle events involve concerted conformational changes in the TL, and potentially the BH[12-14,19-23]. The extent to which these conformations are supported by, or communicate with, the surrounding enzymatic context can be examined by structural or computational approaches, but functional importance needs to be determined experimentally. The BH is straight in most msRNAP structures[7,8,12,13,24], but appears kinked in *Thermus thermophilus* (bacteria) RNAP[5,25]. Simulations suggest these dynamics may promote msRNAP translocation[16,25-28]. The TL adopts various conformations to support its multiple functions. During each NAC, the TL nucleotide interaction region (NIR) discriminates correct NTPs from mismatched ones, initiating a shift from a catalytic-disfavoring “open” state to a catalytic-favoring “closed” state[11,20,29,30]. This closure promotes catalysis[20,31], and subsequent TL reopening is proposed to support polymerase translocation to the next template DNA position, allowing for the next NAC[32-34](**Fig. 1a**). Disrupting the TL with mutations affects transcription at all stages[13,17,23,35-39]. For instance, NIR mutations impair TL-substrate interactions, resulting in reduced catalysis and elongation rate in vitro (Loss of function, LOF)[17,23,36,37,40,41]. Mutations in the TL hinge and C-terminal regions appear to shift the TL toward the active state, enhancing catalysis and elongation rate but impairing transcription fidelity (Gain of function, GOF)[17,42,43]. Mutations may also affect other transcription processes such as proofreading, pausing and termination[12,43-46], as TL confirmations are associated with these activities in addition to catalysis and translocation.

All TL conformational dynamics and functions are likely balanced by residue interactions within and around the TL[41,45,47-49]. Embedded in the conserved active site, the TL interacts with surrounding domains such as the BH and α46-47 helices, forming a five-helix bundle enclosing a hydrophobic pocket that supports these dynamics **(Fig. 1a)**[12,42]. Mutations in TL adjacent domains (e.g., BH GOF T834P and LOF T834A, funnel helix α-21 GOF S713P, and Rpb2 GOF Y769F)[17,23,25,26,35-37] **(Fig. 1a)**, and in a Pol II subunit which does not directly contact Pol II active site, such as Rpb9[50], also alter catalytic activity and fidelity, showing phenotypes seemingly identical to TL mutants, indicating that TL dynamics and function are finely balanced and could be sensitive to allosteric effects[50-53]. Determining the extent and nature of the pathways connecting the TL to the rest of the polymerase will reveal the functional networks that shape its dynamics and the potential pathways through which Pol II has evolved or may be controlled by elongation factors.

Physical and functional intramolecular interactions between amino acids define protein function and evolvability[54-57]. Epistasis, where mutant phenotypes depend on the identities of other amino acids, contributes to protein evolvability by providing a physical context and an evolutionary window in which some intolerable mutations may be tolerated[58-60]. Recent studies

have shown how mutations can alter protein function, allostery, and evolvability, suggesting that even conserved residues are subject to unique, context dependent epistatic constraints[61-68]. Consistent with this, distinct phenotypes for the same conserved residues have been observed in various proteins, including yeast Pol I and Pol II[66,67,69]. For example, the TL domain of yeast Pol I is incompatible with Pol II, despite sharing 70% of sequence identity, while the similarly distinct Pol III TL maintains some function[70]. It is not known generally if highly conserved TL sequences are compatible in a heterologous msRNAP context. Answering this question would reveal how tightly integrated the TL is by coevolution with its embedded context, or the extent to which its functions are self-contained due to its very high conservation.

Functional interactions between residues can be revealed by genetic interactions of double mutants[17,37,71-73]. A systematic analysis is needed to fully describe and understand the requirements for each mutant's phenotype, and the nature of the interactions that control Pol II activity. Previous studies from our lab on a small subset of site-directed substitutions identified distinct types of Pol II double mutant interactions, including suppression, enhancement, epistasis, and sign-epistasis[17,37,72]. Suppression was common between LOF and GOF mutants, as expected if each mutant is individually acting in the double mutant, balancing opposing effects on activity. Similarly, synthetic sickness and lethality were common between mutants of the same class (GOF or LOF), consistent with greater defects arising from combining partial losses of TL function. However, we also observed lack of enhancement between mutants of the same class (epistasis), suggesting these mutants might act at the same step. Additionally, we observed a potential case of sign-epistasis, where a mutant's phenotype class appeared dependent on the identity of another residue. For example, the GOF TL substitution Rpb1 F1084I was unexpectedly lethal with the LOF TL substitution Rpb1 H1085Y, contrary to the predicted mutual suppression for a GOF/LOF combination[37,72]. This suggested that F1084I required H1085 for its GOF characteristics and became a LOF mutant in the presence of H1085Y (**Fig. 1b**).

Deducing large-scale residue interaction networks is challenging. To accomplish this for Pol II, we developed experimental and analytical schemes to extend the previously established "Pol II phenotypic landscape"[17,37,72,74] to 15,174 double and multiple mutants within the *S. cerevisiae* Pol II TL and between the TL and adjacent domains (a "Pol II Interaction landscape"). Our analyses indicate that TL function and evolution are dominated by widespread epistasis. The TL faces extensive constraints despite its high conservation, arising from residues within the TL and its interacting domains, resulting in highly similar TLs being incompatible inside yeast Pol II to a large degree. Additionally, individual mutants with similar biochemical and genetic phenotypes have quite distinct genetic interaction networks, revealing differential functional requirements for their abilities to confer altered Pol II activities. Some mutants minimally change the genetic behavior of most TL substitutions when combined, suggesting that TL conformations or interactions remain largely unchanged, with altered TL dynamics hypothesized to be the sole difference. In contrast, other alleles greatly perturb the genetic behavior of many TL substitutions, indicating these substitutions change the active site landscape in ways that would otherwise undetectable. Together, these results suggest small changes in the Pol II active site can dramatically change its constraints and therefore, its potential evolutionary paths. Furthermore, our findings highlight potential communication networks through evolutionary coupling of Pol II residues within the active site, which may underlie allosteric communication paths to the active site for elongation factors.

RESULTS

A system for dissection of the Pol II active site genetic interaction landscape. We developed an experimental and analytical framework, termed the Pol II TL interaction landscape, to dissect residue interactions that shape Pol II TL function and evolution in *S. cerevisiae*. We designed and synthesized 15,174 variants representing evolutionary haplotypes, all possible Pol II TL single mutants and a subset of targeted double mutants in ten libraries (Supplemental Table 1). This approach follows our prior analysis of the TL phenotypic landscape[17] with modifications (**Methods** and **Extended Data Fig. 1a**). Libraries were transformed, screened under selected conditions (**Methods**), and sequenced (**Fig. 1c, Extended Data Fig. 1a**). Mutant growth phenotypes are calculated based on relative allele frequency shifts compared to a control condition and normalized to the WT under identical conditions. Biological replicates indicate high reproducibility (**Extended Data Fig. 1b-c**). Individual libraries were min-max normalized[75] to account for scaling differences between libraries (**Fig. S1a**) and the same mutants present among different libraries indicate high correlation of fitness determinations in each library (**Fig. S1b-c**).

We defined a conceptual framework for evaluating genetic interactions among TL mutations. First, we assume that independent mutant effects combine in log-additive manner. This means that predicted double mutant fitness defects should be the combination of both single mutant defects, as is standardly assumed[60,71,73,76]. Deviations from log-additive expectations represent genetic interactions: either less than expected (i.e. suppression) or more than expected (i.e. synthetic sickness or lethality). Importantly, our phenotyping analyses determine both general mutant fitness and predict their class of in vitro biochemical defect. Our previous studies showed that phenotypic profiles from conditional growth assays, reflecting Pol II-activity dependent phenotypes, correlate with the in vitro biochemical activity of purified mutant Pol II complexes[17,37]. By classifying Pol II active site mutants as “GOF” or “LOF” based on predicted in vitro biochemical phenotypes, we establish baseline expectations for their genetic interactions. We previously observed activity additive interactions, meaning suppression between mutants of different classes (GOF+LOF) or synthetic sickness/lethality within the same class (GOF+GOF or LOF+LOF). To distinguish specific epistatic interactions from activity-dependent effects, we defined an interaction as epistasis when we observed positive fitness deviation in mutants of the same activity class (GOF+GOF, LOF+LOF), where we would otherwise expect synthetic sickness or lethality if mutants were functioning independently. Conversely, we defined sign epistasis for situations where negative deviations in combinations between the classes (GOF+LOF), where suppression would be expected for independent mutants (**Fig. 1d, Extended Data Fig. 2**).

The Pol II active site interaction landscape relies on accurate classification of mutant classes. Using the established correlation between growth profiles and in vitro catalytic effects[17,37], we trained two multiple logistic regression models to distinguish GOF and LOF classes (**Extended Data Fig. 3a**) and models were applied to all viable mutants (growth fitness score > -6.5), classifying the mutants into three groups, GOF, LOF and unclassified (mutants not belonging to either class). To visually inspect the classifications, we applied t-SNE projection and k-means clustering for all measured mutants. We observed separated GOF and LOF clusters consistent with logistic regression classifications (**Extended Data Fig. 3b-c**). Notably, mutants with similar defects are further separated into different clusters, suggesting their similar phenotypic defects may be related to different transcription defects (**Extended Data Fig. 3c**).

We compared interactions observed in sequencing to growth assays for 59 previously examined double mutants[17,37], with 48 matching our observations. The other 11 were categorized as ultra-sick/lethal and therefore inaccessible to sequencing analysis (Supplemental Table 2). We constructed 63 additional mutants to assess interactions by patch assay and spot assay, and these aligned with our high-throughput results (**Extended Data Fig. 4**).

Widespread incompatibility of conserved TL sequences with yeast Pol II suggests the TL is highly constrained by its coevolved environment. We previously found that identical mutations in a residue conserved between the Pol I and Pol II TLs yielded different biochemical phenotypes[70,77]. Additionally, the yeast Pol I TL was incompatible within the yeast Pol II enzyme, implying that TL function in that case depended on its enzymatic context[70,77]. To determine the scope of TL-Pol II incompatibility, we designed a library containing evolutionary TL variants from bacterial, archaeal, and eukaryotic msRNAPs and determined their compatibility in the yeast Pol II context (**Fig. 2a**). Eukaryotic TL alleles were more compatible than those from archaea or bacteria, with Pol II alleles being the most compatible (**Fig. 2b, Extended Data Fig. 5a-b**), consistent with evolutionary distance. Growth fitness in the Pol II background showed a slight negative correlation with the number of TL substitutions for most TLs but not those from bacteria (**Extended Data Fig. 5c**), likely because of the bacterial TLs being largely incompatible with Pol II. Despite this, some archaeal TLs provide yeast Pol II viability, yet several Pol II TLs were defective or lethal. These results suggest widespread coevolution between TL sequences and that the enzymatic background, beyond ultra-conserved positions, shapes TL function in individual enzymes. We have explored the nature of this incompatibility and complex intra-TL genetic interactions further in a separate study[78].

Allele-specific interactions suggest unique properties of individual mutants with similar phenotypes. To determine the potential residue interactions surrounding the TL in the yeast Pol II environment, we analyzed 12 previously studied GOF and LOF mutants (eight within the TL and four outside), each combined with >600 perturbations in the form of all single substitution TL mutants (**Fig. 3a**). These 12 mutants can be envisioned to function as probes for the genetic interaction space of the TL and how it might be altered in allele-specific fashion by perturbation by the “probe” mutation. Importantly, TL conformational dynamics and function are balanced by internal residue interactions within the TL and by TL-external interactions between the TL and TL-proximal domains. While GOF and LOF mutants in TL-adjacent domains appear similar to GOF and LOF TL mutants, their underlying mechanisms or specific residue dependencies are not known. We therefore compared interaction networks among probe mutants with similar biochemical and phenotypic defects to distinguish if changes to TL function might reflect simple alterations to TL dynamics, or additional alterations to folding trajectories or conformations.

We observed distinct interaction networks among probe mutants, even for those with similar apparent biochemical defects (**Fig. 3b-d**), indicating that mutants differentially impact the Pol II active site, potentially reflective of different constraints and distinct properties, as discussed below. A simple expectation is that mutants with altered TL dynamics yet maintenance of conformational states should show additive interactions, because the effects of substitutions on function would be maintained. In contrast, substitutions altering TL conformations/folding or propagating changes across the active site, may be subject to allele-specific epistasis. We observed that most probe mutants were placed on continuum of effects based on the balance between additive (independent) interactions and epistatic (dependent or allele-specific) interactions in double mutants, which we interpret as the degree to which they propagate their

222 effects across the active site (**Fig. 3b-c, Extended Data Fig. 6, and Fig. S2**). Probe mutants
223 appeared separable based the extents of their additive or epistatic interactions, where greater
224 numbers of independent additive interactions would indicate fewer effects on other residues'
225 functions. In contrast, greater sign epistatic interactions would indicate greater changes in other
226 mutant's characters and presumably residue function. Specific dependence of mutant
227 phenotypes based on residue identity at other positions is reflected by 127/620 TL substitutions
228 showing unique interactions with specific probe mutants and not sharing interactions based on
229 biochemical/genetic class. For example, some lethal substitutions were suppressed only by
230 Y769F, a GOF TL-proximal Rpb2 mutant (**Extended Data Fig. 7**). Moreover, two TL-adjacent
231 GOF mutants, Rpb1 S713P (funnel α-helix 21) and T834P (BH) displayed largely distinct
232 interaction networks despite similarly increased biochemical activity and genetic phenotypes as
233 single mutants **(Fig 3c, Extended Data Fig. 8a)**. S713P broadly suppressed LOF TL
234 substitutions (96 instances), consistent with generic enhancement and preservation of TL
235 dynamics or residue function. In contrast, T834P exhibited sparser suppression (33 instances)
236 but much greater sign epistasis than S713P (102 versus 38 instances), especially with P1099,
237 where all substitutions showed sign epistasis with T834P but not S713P (**Extended Data Fig.
238 8a**). These results suggest that T834P's GOF function requires most TL residues to be WT, is
239 especially reliant on proline at 1099, and that T834P alteration to the BH extensively changes
240 the TL's functional space, likely through folding or altered conformations.

241 A similar distinction was observed between two internal TL GOF mutants, Rpb1 E1103G and
242 F1084I **(Fig. 3c, Extended Data Fig. 8b)**. E1103G showed widespread suppression of LOF TL
243 substitutions (184 instances), consistent with its proposed role in altering TL dynamics to
244 promote TL closure[23,37] and which allows TL mutants to maintain their effects. In contrast,
245 F1084I showed more limited suppression (43 instances) while showing widespread synthetic
246 lethality due to predicted sign epistasis, indicating that F1084I requires many WT residues for
247 GOF characteristics and itself may switch to a LOF upon many additional TL perturbations.

248 The most striking example came from two LOF substitutions at the ultra-conserved Rpb1 H1085
249 **(Extended Data Fig. 8c)**. This histidine, which contacts incoming NTP substrates[5,12], is the
250 target for the Pol II inhibitor α-amanitin[36,79], and promotes catalysis[12,13]. Initial structural data and
251 molecular dynamics simulations suggested that H1085 functions as a general acid for Pol II
252 catalysis[80-83]. Our discovery that H1085L was well-tolerated[17], and subsequent experiments
253 from the Landick lab[84,85], have led to their proposal that the TL histidine functions as a positional
254 catalyst where a similarly sized leucine substitution supports catalysis with mild effects on
255 biochemistry and growth. If H1085Y and L substitutions represent a continuum of positional
256 catalyst activity, then their interaction networks would be expected to be similar, and differing
257 only in magnitude, not identity or type of interactions. Contrary to this, distinct interaction
258 patterns were observed (**Fig. 3c, Extended Data Fig. 8c**). Most GOF mutants suppressed
259 H1085Y but not H1085L. Instead, H1085L showed synthetic lethality with most GOF mutants
260 (putative sign epistasis). For example, almost all substitutions at E1103 showed sign epistasis
261 with H1085L but not H1085Y (**Fig. S2b, Extended Data Fig. 8c**). The distinction between
262 H1085L and H1085Y is further highlighted in PCA analysis (**Fig. 3d**).

263 **Functional and epistatic interactions within the TL hydrophobic pocket tune Pol II
264 activity.** Several allele-specific epistatic interactions were observed, with some of the most
265 extensive occurring between A1076 substitutions and L1101S (**Fig. 4a**), suggesting tight
266 coupling between A1076 and L1101 for Pol II function. These two hydrophobic residues,

together with other hydrophobic residues in TL helices, likely stabilize the open TL conformation through hydrophobic packing of the TL helices (**Fig. 4c**). Consistent with this, another pair of adjacent residues, M1079 and G1097, also showed allele-specific epistasis (**Fig. 4b-c**). Additionally, three GOF/GOF combinations between L1101S and A1076 substitutions showed WT-like behavior for the double mutants based on our regression model for mutants, indicating mutual suppression due to one of the singles switching to a different class (sign epistasis), further supporting a tight functional interaction between 1101 and 1076 (**Fig. S3a**).

We also observed allele-specific interactions for predicted lethal mutants. Our lethality threshold is more conservative than the actual lethal threshold and therefore, some classified lethal but actually slow-growing mutants have enough growth in phenotypic assays for GOF or LOF class determination. Among 21 ultra-sick/lethal TL substitutions predicted as GOF, suppression by LOF mutants was expected and observed (**Fig. S3b**). For example, lethal A1076 substitutions were suppressed by LOF probe mutants, suggesting their severe defects result from strong GOF status. However, some A1076 substitutions were also suppressed by the GOF probe mutant L1101S, indicating allele-specific mutual suppression or sign-epistasis, consistent with A1076-L1101 interactions described above (**Fig. S3c**). Similarly, ultra-sick/lethal LOF substitutions were commonly suppressed by GOF mutants, but some were suppressed by specific LOF mutants (**Fig. S3b**). For example, S1091G was suppressed by most GOF mutants and specifically by the LOF V1094D (**Fig. S3c**), suggesting allele-specific compensation. Furthermore, some lethal mutants exhibited interactions with specific GOF or LOF probe mutants. For example, F1084R, was specifically suppressed by LOF probe Q1078S and GOF probe Y769F (**Fig. S3c**). Notably, F1084, Q1078S and Y769 are in close proximity in the substrate bound, catalytic-favoring TL conformation. These types of allele-specific interactions potentially allow the TL and adjacent residues to evolve and differentiate while maintaining essential functions.

We note that strong epistasis is much more prevalent in the Pol II system than in other quantified proteins[57,86-89] (**Fig. S3d**), likely due to the high rate of suppressive interactions stemming from Pol II mutants' opposing effects on catalysis.

Mapping TL-internal residue interaction networks suggests widespread epistasis within the TL. To determine TL-internal interaction networks, we selected 2-4 substitutions for each TL residue, representing diverse phenotypes (GOF, LOF, lethal, or unclassified), and combined them with the selected substitutions across all other TL positions. This curated set of 3790 double mutants captures potential interactions between any two TL residues (**Fig. 5a**). Observed fitness of these double mutants was compared to predictions from the additive model, revealing widespread deviation from the model (i.e. large interactions)(r^2=0.21), much smaller than the r^2 (about 0.65-0.75) reported in other studies[57,73,86,87,89] (**Fig. 5b**), likely reflecting our selection criteria for mutations with diverse phenotypes. In general, mutations of the same class were additive or exacerbating, with some exceptions that reveal functional dependencies between residues (**Fig. 5c, 5e, Extended Data Fig. 9**). Additionally, the strongest deviations from expectations were between mutations of opposing phenotypic classes (GOF+LOF combinations). Here, commonly we observed suppression as predicted for mutations acting independently in 43% of GOF+LOF combinations but we also observed unexpected lethality or exacerbation (sign epistasis) for 41% of GOF+LOF combinations. Distinct patterns of sign epistasis for GOF/LOF combinations provide the ability to distinguish functional requirements for GOF alleles to be able to confer GOF phenotypes (discussed below). Interactions were

312 distributed throughout the TL, covering every residue, supporting connectivity across the TL
313 (**Fig. 5d**). Notably, epistasis clustered within the C-terminal TL helix and adjacent regions (The
314 far right panel of **Fig. 5d**), supporting functional dependencies of TL-C terminal residues on one
315 another, consistent with their proposed function in collaboratively stabilizing the open TL.

316 **Genetic interactions reveal insights into lethal or unclassified individual mutants.** Most
317 lethal mutants could be suppressed by at least one predicted GOF mutant (**Fig. 5f, Extended**
318 **Data Fig. 9**), suggesting their lethality likely comes from reduced activity (LOF) below a viable
319 threshold. However, this suppressibility also suggests that individual lethal substitution activity
320 defects are mostly close to the viable threshold. This suggests that the contributions of most
321 individual residues represent only a portion of total TL activity, which is expected to provide a
322 ~1000 fold increase in catalytic activity. Suppressibility of lethal residues by GOF alleles is also
323 consistent with the greater probability of lethal substitutions being LOF rather than GOF.
324 However, two lethal mutations at A1076 were suppressed by most LOF mutations or specific
325 lethal mutants, but not GOF mutants, implying that their lethality resulted from being GOF.
326 Additionally, unclassified single mutants generally showed limited interactions with GOF, LOF,
327 or lethal classes, consistent with small or mostly independent effects. However, a few
328 unclassified mutants showed suppression in combination with GOF mutants, suggesting they
329 are either potential atypical LOF not detected by phenotypic analysis, or allele-specific
330 interactions (**Fig. 5g, Extended Data Fig. 9**).

331 We reasoned that evolutionarily observed lethal substitutions would be closer to functional
332 viability than non-observed, and would be therefore more likely to be suppressible by Pol II GOF
333 mutants. To determine this, we compared the suppressibility of substitutions observed in
334 existing msRNAPs that are lethal in *S. cerevisiae* Pol II versus substitutions that are lethal but
335 not present in extant msRNAPs by analyzing the maximum positive deviation scores from all
336 double mutants containing individually lethal substitutions. Singly lethal substitutions identified in
337 our msRNAP TL MSA showed higher maximum deviation scores than absent singly lethal
338 substitutions (**Fig. 6a, Extended Data Fig. 5b**). Consistently, most L1081 substitutions cannot
339 be suppressed, whereas a L1081M, (commonly a WT residue in bacteria and archaeal RNAPs)
340 showed the highest suppressibility (**Fig. 6b**). These results indicate that singly lethal mutants in
341 *S. cerevisiae* Pol II observed elsewhere msRNAP evolution, on average, maintain greater
342 functionality and/or are more easily suppressed by single additional mutants in yeast Pol II.
343 Interestingly, most lethal substitutions in A1087 and all lethal substitutions in G1088 cannot be
344 suppressed (**Fig. 6b**), suggesting the strict restriction at these positions, consistent with the
345 structural observation that A1087 and G1088 are in a small pocket between the bridge and
346 funnel helices[12,17]. The TL has been estimated to enhance catalytic activity by 500-1000 fold [90-
347 92], while yeast viability tolerates only ~10-fold effects[36]. We conclude that lethal mutants
348 observed as functional residues in other species are likely closer to the viability threshold, as
349 might be predicted to result from a series of small adaptive steps that allow their function.

350 **Co-evolution of Pol II active site residues form distinct sectors within specific domains**
351 **and extend to the surfaces of Rpb1 and Rpb2.** Our analyses suggest that even a highly
352 conserved domain like the Pol II TL can be tightly integrated through coevolution of less
353 conserved residues and that substitution tolerance is shaped by widespread epistasis. Changes
354 in residue identities alter interaction networks, shaping the Pol II active site across evolution. To
355 identify the coevolving residue networks in Pol II active site we employed statistical coupling
356 analysis (SCA) for residues within Rpb1 and Rpb2, the two largest subunits of Pol II, which

include the entire active site. SCA is well suited for identifying coupled residue sectors, representing putative residue communication networks[93-95]. From 283 linked Rpb1/Rpb2 sequences, we identified 53 coevolving sectors (**Fig. S4**). Residues within the active site form four major sectors (**Fig. 7a-e**). First, sector 37 includes many Rpb2 link domain residues and most TL residues, including those at the NIR and some at the TL C-terminal (**Fig. 7b**). This sector tightly surrounds the substrate binding pocket (**Extended Data Fig. 10a**), befitting critical roles in catalysis. Second, sector 15 consists of four BH residues, most residues in switch 1 (part of the clamp domain), and many cleft residues, including the α46-47 loop, which accommodates incoming DNA[8,13] (**Fig. 7c**). Residues in this sector directly interact with Pol II subunits Rpb5 and Rpb6 (**Extended Data Fig. 10b**), consistent with Rpb5's role in interacting with the incoming DNA[96]. While the α46-47 loop forms a five-helix bundle with two TL helices and the BH helix[42] (**Fig. 4c**), coupling analysis indicates it is primarily evolutionarily coupled with cleft residues instead of the TL. This suggests that the α46-47 loop may influence TL function by constraining the space for TL movement, rather than directly interacting through specific residue identities. Third, sector 1 involves most active site residues surrounding the Mg^{2+} at the catalytic site and most F-loop residues (**Fig. 7d**). This sector forms a potential communication path that wraps around the TL and BH, connects to the BH through two BH residues, and extends to Rpb9, itself a subunit that forms important inputs to the TL and is required for transcription fidelity[50,97,98]. This pathway likely mediates communication between Rpb9 and the Pol II active site (**Extended Data Fig. 10c**). Fourth, sector 2 contains most BH residues are coupled with the Rpb2 Fork and hybrid binding domain, forming a network linking the BH to Rpb2 residues (**Fig. 7e**). This network connects to Rpb5, which interacts with the downstream DNA, Rpb6, a shared subunit in three eukaryotic msRNAPs, Rpb9, and Rpb3 and Rpb10, which function in Pol II assembly[99] (**Extended Data Fig. 10d**), representing a residue communication path potentially tied to various transcription activities.

Notably, coupling is not restricted to residues that are within or near the active site. Some sectors extend from the active site to the surface of Rpb1/Rpb2 (**Fig. S5a-f**), suggesting that active site function, potentially through the TL, could be modulated by allosteric interactions through the binding of transcription factors. Residues at interfaces with elongation factors can be coupled with those factors yet some residues at interfaces can be coupled with residues distal to the interface, suggesting potential pathways for allosteric interactions. Examples of these are shown for TFIIS (**Fig. S6**), LEO1 (Leo1), ELOF1 (Elf1), and SUPT5H (Spt5) (**Fig. S7**). Together, our findings highlight potential communication networks through evolutionary coupling that may underlie regulation paths from Pol II surface to active site.

DISCUSSION

How individual mutants alter a protein's function is not necessarily straightforward at the mechanistic level. Amino acid substitutions both remove functionality of the WT residue but replace that functionality with something different. By altering the local environment within a protein or potentially propagating effects to distant locations, each substitution potentially can be quite different. These differences may not be apparent as phenotypic outputs, and phenotypic assays may not have granularity to distinguish different biophysical behaviors if they result in similar outputs. For Pol II mutants, even high-resolution phenotypic analyses, such as gene expression profiling or genetic interaction profiling between Pol II mutants and deletions in other yeast genes[53], suggest that LOF and GOF mutants represent a continuum of defects that match

401 enzymatic activity in vitro. Therefore, these profiles also appear dependent on the output of Pol
402 II activity defects and can't distinguish potential differences in underlying mechanism.

403 Through systematic detection of genetic interactions within the Pol II active site, we have
404 identified functional relationships between amino acids across the TL and between TL
405 substitutions and others. In the absence of double mutant epistasis analyses it would not be
406 possible to differentiate similar alleles from one another. L1101S and E1103G, for example, are
407 two GOF alleles very close to each other in Pol II structure and confer similar phenotypic
408 landscapes across various growth conditions. Here, we find that their distinct interactions
409 support that substitutions at 1101 and 1103 target distinct residue networks (**Fig. 3c, 4a,**
410 **Extended Data Fig. 6, Fig. S2**). L1101 functions in the TL hydrophobic pocket while E1103
411 interacts and co-evolves with a number of TL external residues that together support
412 interactions that maintain the open TL conformation. We also observed connections between TL
413 C-terminal residues that suggest a limit to how disruptions to structure there can alter Pol II
414 activity (**Fig. 5d**). Helix-disrupting LOF proline substitutions in at least two TL positions showed
415 epistasis with multiple substitutions in the back of the TL (1094-1098), suggesting that their
416 functions require TL C-terminal helix structure and in the absence of that structure (proline
417 disruption) effects are no longer additive.

418 The strongest epistatic interactions were observed between two pairs of hydrophobic residues,
419 A1076 and L1101, and M1079 and G1097 (**Fig. 4**), suggesting their interdependence in
420 maintaining TL open conformation stability[42]. Considering the TL's multiple active site roles, the
421 observed interaction networks may also contribute to other NAC steps or off pathway steps (*eg.*
422 pausing or backtracking). Structural studies have proposed that these hydrophobic residues
423 form a pocket stabilizing the TL by bundling two TL helices with the BH and α46-47 loop in a
424 five-helix bundle[28,42]. However, our coupling analysis suggests that α46-47 loop is evolutionarily
425 coupled with cleft residues rather than the TL, indicating the α46-47 loop may indirectly impact
426 TL function by limiting the space available for TL movement, rather than through direct
427 interactions with TL residues (**Fig. 7c**).

428 Elongation factors bind Pol II and alter its activity, but the mechanisms by which they do so are
429 not known[100,101]. We observed a high level of genetic interactions between residues outside the
430 TL and residues within it, including allele-specific reshaping of TL mutant space upon single
431 substitution outside the TL (**Fig. 3**). The fact that minor mutational changes outside the TL can
432 apparently functionally perturb the TL would be consistent with the idea that minor alterations to
433 Pol II structure upon elongation factor binding could easily propagate into the active site via the
434 TL or the BH. As an example, human Rtf1 has been observed to project a domain into the Pol II
435 structure adjacent to the BH (in yeast, this region is occupied instead by Rpb2[102]). These
436 contacts have been proposed to alter Pol II activity. We would propose that the paths for such
437 alteration to activity may follow the coupling sectors we have observed by SCA (**Fig. 7**).

438 How different individual substitutions are under the surface is critical for understanding plasticity
439 in protein mechanisms and how they might be altered by evolutionary change. A key open
440 question in nucleic acid polymerase mechanisms is the paths for protons in the reaction (for
441 example, deprotonation of the synthesized strand 3′-OH and protonation of pyrophosphate
442 leaving group, for example[80,81,83,85,103-105]). For msRNAPs, the association with the incoming NTP
443 by a universally conserved histidine led to the proposal that this residue might donate a proton
444 during the reaction [12,82,103]. Some substitutions at this position can provide minimal essential
445 function (e.g. tyrosine, arginine), while others are only moderately defective (glutamine).

446 Surprisingly, we found that H1085L was very-well tolerated for growth [17] and the Landick lab
447 has proposed this substitution supports catalysis through positional but not chemical effects[84,85].
448 Our studies here were quite surprising in that they indicated that L1085 Pol II has unique
449 behavior when perturbed by all possible TL substitutions and is entirely distinct from H1085Y
450 (where we have direct observations of all possible intra-TL doubles) or H1085A or H1085Q
451 (curated doubles) (**Extended Data Fig. 8c, Fig. S8**). These residue specific behaviors suggest
452 that each substitution may have different properties, and compatibility with function may not
453 necessarily represent similar function under the surface.

454 Evolutionary change over time can alter protein function but it can also alter protein functional
455 plasticity. Recent work from the Thornton lab elegantly demonstrates that phenotypes of
456 substitutions to residues conserved over hundreds of millions of years can change over
457 evolutionary time and can do so unpredictably and transiently during evolution[62]. msRNAPs
458 have structures and functions conserved over billions of years, and deep within their active sites
459 is a mobile domain, the TL, that has large functional constraints on its sequence. The TL
460 sequence must be able to fold into multiple states and maintain recognition of the same
461 substrates across evolutionary space and is shows high identity even between distantly related
462 species. Here we show that the TL, and likely the entire Pol II active site, exhibits a great
463 amount of plasticity through non-conserved positions that are essential for compatibility of the
464 TL and surrounding domains. A limitation of our study is its reliance primarily on genetic and
465 statistical coupling analysis. Future biochemical and biophysical studies will give mechanistic
466 insight into the activity defects underlying the functional connections we observe, for example
467 connecting kinetic properties or structural states to specific mutants. Nonetheless, our results
468 illustrating widespread epistasis and allele-specific effects of single and double mutants predict
469 that comparative analyses among Pol I, II, and III will reveal shared but also enzyme-specific
470 mechanisms due to higher order epistasis shaping the functions of conserved residues.

471 **METHODS**

472 **Design and Synthesis of TL mutant libraries.** We updated and extended the fitness dataset
473 of Qiu *et al*[17]. Using a similar methodology, but with adjusted conditions and a second-
474 generation mutant library strategy to generate a complete Pol II TL mutation-phenotype map
475 and examine genetic interactions. Mutants were constructed by oligo synthesis (Agilent) and
476 screened for phenotypes previously established as informative for Pol II mutant biochemical
477 defects. Programmed oligonucleotide library pools included all 620 single TL residue
478 substitutions and deletions for Rpb1 amino acids 1076-1106 (Library 1), 3914 pairwise double
479 substitutions (Library 2), 4800 targeted double substitutions (Library 6), and 3373 multiple
480 substitutions (Library 3-5), along with the WT *S. cerevisiae* Pol II TL allele at a level of ~15% of
481 the total variants, enabling precise quantification (see Supplemental Table 1, 3). Each
482 synthesized region contained a mutated or WT Pol II TL sequence and two flanking regions at
483 the 5′ and 3’ ends of the TL-encoding sequence. These flanking regions also contained
484 designed “PCR handle” (20bp) sequences, allowing distinct subsets of oligos to be amplified
485 from synthesized pools using selected primers for PCR, and additional flanking WT Pol II
486 sequences allow for further extension of homology arms by PCR “sewing” (Details are in
487 Supplemental Method 3).

488 **Introduction of Libraries into yeast**. Synthesized mutant pools were transformed into yeast
489 (CKY283) along with an *RPB1*-encoding plasmid where the TL-encoding sequence was
490 replaced with an *Mlu*I restriction site for linearization as described in Qiu et al[17]. This strategy

allows construction of *rpb1* mutant libraries by gap repair between library fragments and the linearized vector. Briefly, the synthesized oligo pools were amplified by limited cycles of emulsion PCR to limit template switching. Extension of flanking homology arms of ~200 bp were added by PCR sewing. Amplified TL sequences with extended flanking regions were co-transformed with linearized pRS315-derived *CEN LEU2* plasmid (pCK892) into CKY283, allowing gap repair via homologous flanking regions. To detect potential residue-residue interactions between the TL and TL-proximal domains including the Rpb1 Bridge Helix (BH), Funnel Helix alpha-21 and Rpb2, the Pol II TL single mutant pool (Library 1, 620 mutant alleles and 111 WT alleles) was co-transformed individually with gapped plasmids encoding an additional *rpb1* allele (Rpb1 BH T834P, T834A, or Funnel Helix alpha-21 S713P) into CKY283 respectively, or with the gapped WT *RPB1* plasmid into a strain with the genomic mutation, *rpb2* Y769F. These co-transformations created double mutants between the TL and TL-proximal mutants. The WT allele in single mutant pool represented the single probe mutant due to substitutions outside the TL on the plasmid or in the strain background. To distinguish between a fully WT TL and a WT TL representing the TL of a mutant allele elsewhere, a WT Pol II TL allele with a silent mutant at T1083 (WT codon ACC was replaced with ACT) was co-transformed with plasmid containing gapped WT *RPB1* in a WT strain in parallel. 15% of the transformants with silent mutation were mixed with transformants of double mutants. The silent mutation allowed us to distinguish the WT and the single mutants.

Phenotyping libraries with different conditions. Each transformation was done in three biological replicates. After transformation, Leu^+ colonies were collected from **SC-Leu** plates and replated on **SC-Leu+5FOA** to select for cells having lost the *RPB1 URA3* plasmid and to measure growth defects. 5-FOA-resistant colonies were then scraped and replated on different conditions to assess functional differences between WT, GOF, and LOF mutants[17,37]. **SC-Leu + 20 µg/L MPA** (Fisher Scientific) evaluates transcription start site (TSS) shifting. MPA depletes GTP levels in yeast. To generate GTP, *IMD2* expression is required, but its promoter has multiple transcription start sites (TSS)[106,107]. Transcripts from the downstream TSS express functional *IMD2* upon MPA treatment. WT and LOF mutants are resistant to MPA due to their ability to use downstream TSSs for *IMD2* expression, while GOF mutants are sensitive as they can only use upstream TSS sand fail to express functional *IMD2*[53,108]. **SC-Leu + 15 mM Mn** (Sigma): Mn^{2+} compromises transcription fidelity[109] and likely also increases Pol II catalysis; while WT and LOF mutants are resistant, GOF mutants are sensitive either due to decreased fidelity or exacerbated catalytic increase. **YPRaf** and **YPRafGal**: the *gal10Δ56* allele compromised *GAL10* 3'-end formation and polyadenylation, leading to transcription read-through that inhibits the downstream *GAL7* gene [110,111]. The transcription readthrough in WT *gal10Δ56* cells leads to accumulation of a toxic galactose metabolite because of defects in *GAL7* expression. Some GOF and most LOF mutants show varying galactose resistance, likely through increasing termination in the *GAL10-GAL7* intergenic region or otherwise reducing read-through interference with *GAL7*. YPRaf serves as a control for YPRafGal, to demonstrate that the defect on YPRafGal is galactose toxicity. **SC-Lys** tests lysine auxotrophy. The *lys2-122∂* allele in the strain background has a *Ty1* transposable element insertion, which prevents normal expression of *LYS2*[112]. WT and LOF mutants are Lys^-, while GOF mutants utilize a normally silent promoter within the *Ty1 ∂* element insertion, becoming Lys^+. **SC-Leu + 3% formamide** (JT Baker), formamide destabilizes protein hydrogen bonds[113], with most mutants showing resistance except for slight sensitivity in LOF mutants. Details of cell numbers plated

536 on each plate and screening time of each plate are in Supplemental Table 5. Details of the high
537 efficiency transformation protocol are in Supplemental Method 1.

538 **Generation of libraries for quantification by amplicon sequencing**. Genomic DNA of each
539 screened library was extracted using the Yeastar genomic DNA kit according to manufacturer's
540 instructions (Zymo Research). To ensure adequate DNA for sequencing, the TL regions of all
541 libraries were amplified with PCR cycles that were verified to be in the linear range by qPCR to
542 minimize disturbance of allele distributions, and under emulsion PCR conditions (EURx
543 Micellula DNA Emulsion & Purification (ePCR) PCR kit) to limit template switching. Details are in
544 Supplemental Method 2 and 3. To multiplex samples, we employed a dual indexing strategy
545 wherein 10 initial barcodes for differentiating 10 mutant libraries were added during the initial
546 amplification using 10 pairs of custom primers. In a second amplification, 28 primers containing
547 28 NEB indices were used to add a second index for distinguishing conditions and replicates
548 (NEBNext Multiplex Oligos for Illumina) (see Supplemental Table 4). As a result, a sample-
549 specific barcodes were present for each set of variants. The indexed, pooled samples were
550 sequenced by single end sequencing on an Illumina Next-Seq (150nt reads). On average, over
551 11 million reads were obtained for individual samples with high reproducibility from two rounds
552 of sequencing.

553 **Data cleaning and fitness calculation and normalization**. Reads of mutants were sorted into
554 appropriate libraries and conditions by detecting particular indices after sequencing. Read
555 counts were estimated by a codon-based alignment algorithm to distinguish reads that exactly
556 matched designated codons of mutants [114]. To clean the data, mutant reads with coefficients of
557 variation greater than 0.5 in the control condition (SC-Leu) were excluded from the analysis.
558 The mutant read count was increased by 1 to calculate the allele frequency under different
559 conditions. To measure and compare the phenotypes of all mutants, mutant phenotypic score
560 (fitness) was calculated by allele frequency change of a mutant under selective conditions
561 relative to the unselective condition comparing to the frequency change of WT. The formula for
562 calculating fitness is shown below.

563 Fitness (mut) = $\log [f^{mut, sele} / f^{mut, unsele}$ - $\log [f^{WT, sele} / f^{WT, unsele}]$

564 We applied min-max normalization to bring the median growth fitness of mutants measured at
565 ten libraries to the same level for direct comparison (formula is shown below). In each library,
566 we divided mutants into several groups based on their allele counts on the control condition.
567 Mutants with read count differences of less than 10 are present in one group. The WT growth
568 fitness was set as the maximum value and the minimum fitness in each group was the
569 minimum. Min-max normalization was used to equalize the growth fitness into the same range
570 between various groups inside each library. Additionally, we utilized min-max normalization to
571 level the mutant fitness across all ten libraries with WT fitness as Max and minimal fitness in
572 each library as the minimum. As a result, mutant growth fitness was scaled to one range and
573 could be used to determine genetic interactions.

574 $$X' = \frac{X - Xmin}{Xmax - Xmin}$$

575 **Determination of functional interactions.** The genetic interactions between single
576 substitutions were determined by comparing the multiple-substitution mutant normalized median
577 fitness to the log additive of the single substitution normalized median fitness. The simplified
578 formula is as follows:

Deviation score ($M_1M_2M_3$) = Fitness ($M_1M_2M_3$) – [Fitness (M_1) + Fitness (M_1) + Fitness (M_3)]

(1). -1 < Deviation score < 1, the interaction among the constituent single mutants is additive and mutants are acting independently.

(2). Deviation score ≥ 1, the interaction is non-additive and is positive, including suppression and epistatic interactions.

(3). Deviation score ≤ -1. the interaction is non-additive and is negative, including synthetic sick, synthetic lethal, and sign epistasis interactions.

Any mutation with fitness smaller than the lethal threshold (-6.50) was classified as an ultra-sick/ lethal mutant and its fitness was normalized to -6.50 for calculation of the deviation score. Synthetic sickness and synthetic lethality were distinguished by whether a double mutant is viable or lethal (fitness is greater than or equals to the lethal threshold -6.5) when two constituent mutations are viable. Synthetic lethality can be further classified into two types. First, additive-synthetic lethality was determined when the expected double mutant fitness calculated by additive model was lethal (expected fitness = -6.5) and the observed double mutant fitness was also lethal (fitness = -6.5) (in this case the deviation score = 0). Second, the beyond-additive synthetic lethality was determined when the expected double mutant was viable (expected fitness > -6.5) while the observed double mutant fitness was lethal (fitness = -6.5) (in this case the deviation score < 0). To separate these two situations in our figures, we labeled additive synthetic lethality as black and beyond-additive synthetic lethality as purple. Details of formulas are in Supplemental Method 4.

Mutant classification using two multiple logistic regression models. We trained two multiple logistic regression models to distinguish GOF and LOF mutants using phenotypic fitness from SC-Leu+MPA, SC-Lys, and YPRafGal conditions of 65 single mutants. This dataset included 20 mutants with transcription rates measured by biochemical experiments (13 GOF and seven LOF)[17,37,53], and 45 additional mutants that were hierarchical clustered with verified mutants (12 GOF, 26 LOF, 1 WT, and 6 that were not GOF or LOF mutants)[17]. Both models incorporated intercept, main effects, and two-way interactions were involved in defining both models, with a cutoff threshold of 0.75 applied to classify mutants in both of the GOF and LOF models.

Model for predicting the probability of a mutant being a GOF:

$$y = \frac{1}{1 + e\text{^}(1.816 + 2.542 * fMPA - 1.942 * fLys + 0.06566 * fGal - 0.5297 * fMPA * fLys - 0.08373 * fMPA * fGal + 0.02556 * fLys * fGal)}$$

Model for predicting the probability of a mutant being LOF:

$$y = \frac{1}{1 + e\text{^}(1.916 - 1.392 * fMPA - 1.328 * fLys - 0.8353 * fGal - 0.01112 * fMPA * fLys - 0.2992 * fMPA * fGal + 0.8823 * fLys * fGal)}$$

Both models showed accuracy, with the area under ROC close to one **(Extended Data Fig. 2A)**. The details are provided in Supplemental Table 6.

Principal component analysis (PCA). Deviation scores of curated and probe double mutants were analyzed in PCA. The scripts used R language v4.0.3 (https://www.R-project.org/) with R packages tidyverse v1.3.1 (https://www.tidyverse.org), prompt (stats v3.6.2 (https://www.rdocumentation.org/packages/stats/versions/3.6.2/topics/prcomp)), ggplot2 v3.3.3

620 (https://ggplot2.tidyverse.org), dplyr v1.0.6 (https://dplyr.tidyverse.org), and missMDA v1.18
621 (https://dplyr.tidyverse.org).

622 **t-SNE projection.** Allele frequencies for all mutants in nine conditions with three replicates were
623 analyzed by t-SNE (Perplexity = 50) or k-means (clusters =20). Thirteen clusters with ultra-sick
624 to lethal mutants as majority were eliminated. The remaining mutants were analyzed again with
625 t-SNE (Perplexity = 100) and k-means (cluster =10). The scripts utilized R language v4.0.3
626 (https://www.R-project.org/), along with R packages Rtsne v0.15
627 (https://github.com/jkrijthe/Rtsne), ggplot2 v3.3.3 (https://ggplot2.tidyverse.org), k-means (stats
628 v3.6.2 (https://www.rdocumentation.org/packages/stats/versions/3.6.2/topics/kmeans)).

629 **Statistical coupling analysis.** 5787 eukaryotic homologous sequences of yeast Rpb1 from a
630 published multiple sequence alignment (MSA) and 4000 Rpb2 sequences from NCBI nr
631 database were cleaned and used in the statistical coupling analysis[85]. Sequence identity was
632 reducing to 90% with T-coffee package v12.00.7fb08c2[115]. Pol I, II, and III sequences were
633 separated based on a phylogenetic tree constructed with FastTree 2[116]. Finally, 283 matched
634 Pol II Rpb1 and Rpb2 sequences, with each matched pair sharing the same species name,
635 were connected with 10 Ns and aligned with T-coffee. This newly generated MSA was used for
636 statistical coupling analysis with the python-based package pySCA v6.1[94]. The scripts were
637 adapted from https://github.com/ranganathanlab/pySCA.

638 **Supplemental Tables**

639 Supplemental Table 1. Library summary

640 Supplemental Table 2. Double mutant interactions observed in high throughput system and
641 growth assays in published papers

642 Supplemental Table 3. Strains and plasmids

643 Supplemental Table 4. Primers

644 Supplemental Table 5. Phenotyping details

645 Supplemental Table 6. MLR_models_summary

646 Supplemental Table 7. Kruskal-Wallis tests

647 **Supplemental methods**

648 Supplemental Method 1. High efficiency large scale chemical yeast transformation protocol.

649 Supplemental Method 2. Emulsion PCR set up with EURx Micellula DNA Emulsion &
650 Purification (ePCR) PCR kit.

651 Supplemental Method 3. Amplification/transformation/screening of mutant libraries and
652 sequencing pool preparation.

653 Supplemental Method 4. Formulas of calculating functional interactions.

654 **ACKNOWLEDGMENTS**

655 We thank Dr. Anne-Ruxandra Carvunis (U. Pittsburgh) and Dr. Steve Lockless (Texas A&M) for
656 discussions and advice. We thank Zhizhen Wang and Muyao Lin from the Pitt Statistical

Consulting Center for their advice on checking the reproducibility of our data. We acknowledge funding from NIH R01GM097260 for initiation of this project and NIH R35GM144116 for this work. This research was supported in part by the University of Pittsburgh Center for Research Computing, RRID:SCR_022735, through the resources provided. Specifically, this work used the HTC cluster, which is supported by NIH award number S10OD028483.

AUTHOR CONTRIBUTIONS

BD performed sequencing library construction, data analysis, and made figures, drafted and revised the manuscript. CQ designed the mutant libraries, performed screening experiments and statistical coupling analysis, and contributed to revise the manuscript. SZ counted the mutants from raw sequencing data. CDK conceived the project, guided analyses and interpretation of data, provided funding, revised the manuscript.

COMPETING INTERESTS

The authors declare no conflict of interest.

DATA AVAILIABILITY

Raw sequencing data has been deposited on the NCBI SRA (Sequence Read Archive) database under BioProject PRJNA948661. Processed mutant count, fitness and processing codes are available through GitHub (https://github.com/Kaplan-Lab-Pitt/TLs_Screening.git). Strains and plasmids will be provided upon request.

CODE AVAILIABILITY

The codes for calculating deviation scores, PCA, t-SNE projection, statistical coupling analysis, and generating figures are available in GitHub (https://github.com/Kaplan-Lab-Pitt/TLs_Screening.git).

REFERENCES

1. Cramer, P. Multisubunit RNA polymerases. *Curr Opin Struct Biol* **12**, 89-97 (2002).
2. Werner, F. & Grohmann, D. Evolution of multisubunit RNA polymerases in the three domains of life. *Nat Rev Microbiol* **9**, 85-98 (2011).
3. Allison, L.A., Moyle, M., Shales, M. & Ingles, C.J. Extensive homology among the largest subunits of eukaryotic and prokaryotic RNA polymerases. *Cell* **42**, 599-610 (1985).
4. Zhang, G. et al. Crystal Structure of Thermus aquaticus Core RNA Polymerase at 3.3 Å Resolution. *Cell* **98**, 811-824 (1999).
5. Vassylyev, D.G. et al. Crystal structure of a bacterial RNA polymerase holoenzyme at 2.6 A resolution. *Nature* **417**, 712-9 (2002).
6. Hirata, A., Klein, B.J. & Murakami, K.S. The X-ray crystal structure of RNA polymerase from Archaea. *Nature* **451**, 851-4 (2008).
7. Gnatt, A.L., Cramer, P., Fu, J., Bushnell, D.A. & Kornberg, R.D. Structural basis of transcription: an RNA polymerase II elongation complex at 3.3 A resolution. *Science* **292**, 1876-82 (2001).
8. Cramer, P., Bushnell, D.A. & Kornberg, R.D. Structural basis of transcription: RNA polymerase II at 2.8 angstrom resolution. *Science* **292**, 1863-76 (2001).
9. Fernandez-Tornero, C. et al. Crystal structure of the 14-subunit RNA polymerase I. *Nature* **502**, 644-9 (2013).
10. Hoffmann, N.A. et al. Molecular structures of unbound and transcribing RNA polymerase III. *Nature* **528**, 231-6 (2015).

11. Malinen, A.M. et al. Active site opening and closure control translocation of multisubunit RNA polymerase. *Nucleic Acids Res* **40**, 7442-51 (2012).
12. Wang, D., Bushnell, D.A., Westover, K.D., Kaplan, C.D. & Kornberg, R.D. Structural basis of transcription: role of the trigger loop in substrate specificity and catalysis. *Cell* **127**, 941-54 (2006).
13. Kaplan, C.D. Basic mechanisms of RNA polymerase II activity and alteration of gene expression in Saccharomyces cerevisiae. *Biochimica Et Biophysica Acta-Gene Regulatory Mechanisms* **1829**, 39-54 (2013).
14. Dangkulwanich, M. et al. Complete dissection of transcription elongation reveals slow translocation of RNA polymerase II in a linear ratchet mechanism. *Elife* **2**, e00971 (2013).
15. Bar-Nahum, G. et al. A ratchet mechanism of transcription elongation and its control. *Cell* **120**, 183-93 (2005).
16. Weinzierl, R.O. The nucleotide addition cycle of RNA polymerase is controlled by two molecular hinges in the Bridge Helix domain. *BMC Biol* **8**, 134 (2010).
17. Qiu, C. et al. High-Resolution Phenotypic Landscape of the RNA Polymerase II Trigger Loop. *PLoS Genet* **12**, e1006321 (2016).
18. Da, L.T. et al. Bridge helix bending promotes RNA polymerase II backtracking through a critical and conserved threonine residue. *Nat Commun* **7**, 11244 (2016).
19. Mazumder, A., Lin, M., Kapanidis, A.N. & Ebright, R.H. Closing and opening of the RNA polymerase trigger loop. *Proc Natl Acad Sci U S A* **117**, 15642-15649 (2020).
20. Wang, B., Predeus, A.V., Burton, Z.F. & Feig, M. Energetic and structural details of the trigger-loop closing transition in RNA polymerase II. *Biophys J* **105**, 767-75 (2013).
21. Larson, M.H. et al. Trigger loop dynamics mediate the balance between the transcriptional fidelity and speed of RNA polymerase II. *Proc Natl Acad Sci U S A* **109**, 6555-60 (2012).
22. Fouqueau, T., Zeller, M.E., Cheung, A.C., Cramer, P. & Thomm, M. The RNA polymerase trigger loop functions in all three phases of the transcription cycle. *Nucleic Acids Res* **41**, 7048-59 (2013).
23. Kireeva, M.L. et al. Transient reversal of RNA polymerase II active site closing controls fidelity of transcription elongation. *Mol Cell* **30**, 557-66 (2008).
24. Liu, X., Bushnell, D.A. & Kornberg, R.D. RNA polymerase II transcription: structure and mechanism. *Biochim Biophys Acta* **1829**, 2-8 (2013).
25. Kaplan, C.D. & Kornberg, R.D. A bridge to transcription by RNA polymerase. *J Biol* **7**, 39 (2008).
26. Tan, L., Wiesler, S., Trzaska, D., Carney, H.C. & Weinzierl, R.O. Bridge helix and trigger loop perturbations generate superactive RNA polymerases. *J Biol* **7**, 40 (2008).
27. Silva, D.A. et al. Millisecond dynamics of RNA polymerase II translocation at atomic resolution. *Proc Natl Acad Sci U S A* **111**, 7665-70 (2014).
28. Lin, G. et al. Structural basis of transcription: RNA polymerase II substrate binding and metal coordination using a free-electron laser. *Proc Natl Acad Sci U S A* **121**, e2318527121 (2024).
29. Fong, N. et al. Pre-mRNA splicing is facilitated by an optimal RNA polymerase II elongation rate. *Genes Dev* **28**, 2663-76 (2014).
30. Xu, L. et al. Dissecting the chemical interactions and substrate structural signatures governing RNA polymerase II trigger loop closure by synthetic nucleic acid analogues. *Nucleic Acids Res* **42**, 5863-70 (2014).
31. Vassylyev, D.G. et al. Structural basis for substrate loading in bacterial RNA polymerase. *Nature* **448**, 163-8 (2007).

32. Da, L.T., Wang, D. & Huang, X. Dynamics of pyrophosphate ion release and its coupled trigger loop motion from closed to open state in RNA polymerase II. *J Am Chem Soc* **134**, 2399-406 (2012).
33. Liu, B., Zuo, Y. & Steitz, T.A. Structures of E. coli sigmaS-transcription initiation complexes provide new insights into polymerase mechanism. *Proc Natl Acad Sci U S A* **113**, 4051-6 (2016).
34. Seibold, S.A. et al. Conformational coupling, bridge helix dynamics and active site dehydration in catalysis by RNA polymerase. *Biochim Biophys Acta* **1799**, 575-87 (2010).
35. Malagon, F. et al. Mutations in the Saccharomyces cerevisiae RPB1 gene conferring hypersensitivity to 6-azauracil. *Genetics* **172**, 2201-9 (2006).
36. Kaplan, C.D., Larsson, K.M. & Kornberg, R.D. The RNA polymerase II trigger loop functions in substrate selection and is directly targeted by alpha-amanitin. *Mol Cell* **30**, 547-56 (2008).
37. Kaplan, C.D., Jin, H., Zhang, I.L. & Belyanin, A. Dissection of Pol II trigger loop function and Pol II activity-dependent control of start site selection in vivo. *PLoS Genet* **8**, e1002627 (2012).
38. Matthew H. Larsona, Jing Zhoub,1, Craig D. Kaplanc,1, Murali Palangatd,2, Roger D. Kornberge, Robert Landickd, and Steven M. Blocka,b,f,3. Trigger loop dynamics mediate the balance between the transcriptional fidelity and speed of RNA polymerase II. (2012).
39. Kireeva, M.L. et al. Molecular dynamics and mutational analysis of the catalytic and translocation cycle of RNA polymerase. *BMC Biophys* **5**, 11 (2012).
40. Windgassen, T.A. et al. Trigger-helix folding pathway and SI3 mediate catalysis and hairpin-stabilized pausing by Escherichia coli RNA polymerase. *Nucleic Acids Res* **42**, 12707-21 (2014).
41. Nayak, D., Voss, M., Windgassen, T., Mooney, R.A. & Landick, R. Cys-pair reporters detect a constrained trigger loop in a paused RNA polymerase. *Mol Cell* **50**, 882-93 (2013).
42. Barnes, C.O. et al. Crystal Structure of a Transcribing RNA Polymerase II Complex Reveals a Complete Transcription Bubble. *Mol Cell* **59**, 258-69 (2015).
43. Cheung, A.C. & Cramer, P. Structural basis of RNA polymerase II backtracking, arrest and reactivation. *Nature* **471**, 249-53 (2011).
44. Sydow, J.F. et al. Structural basis of transcription: mismatch-specific fidelity mechanisms and paused RNA polymerase II with frayed RNA. *Mol Cell* **34**, 710-21 (2009).
45. Sekine, S., Murayama, Y., Svetlov, V., Nudler, E. & Yokoyama, S. The ratcheted and ratchetable structural states of RNA polymerase underlie multiple transcriptional functions. *Mol Cell* **57**, 408-21 (2015).
46. Kuldell, J.C. & Kaplan, C.D. RNA Polymerase II Activity Control of Gene Expression and Involvement in Disease. *Journal of Molecular Biology* (2024).
47. Kettenberger, H., Armache, K.J. & Cramer, P. Complete RNA polymerase II elongation complex structure and its interactions with NTP and TFIIS. *Mol Cell* **16**, 955-65 (2004).
48. Lennon, C.W. et al. Direct interactions between the coiled-coil tip of DksA and the trigger loop of RNA polymerase mediate transcriptional regulation. *Genes Dev* **26**, 2634-46 (2012).
49. Hein, P.P. et al. RNA polymerase pausing and nascent-RNA structure formation are linked through clamp-domain movement. *Nat Struct Mol Biol* **21**, 794-802 (2014).
50. Kaster, B.C., Knippa, K.C., Kaplan, C.D. & Peterson, D.O. RNA Polymerase II Trigger Loop Mobility: INDIRECT EFFECTS OF Rpb9. *J Biol Chem* **291**, 14883-95 (2016).
51. Taatjes, A.C.S.a.D.J. Structure and mechanism of the RNA polymerase II transcription machinery. (2020).

52. Leng, X.Y. et al. Organismal benefits of transcription speed control at gene boundaries. *Embo Reports* **21**(2020).
53. Braberg, H. et al. From structure to systems: high-resolution, quantitative genetic analysis of RNA polymerase II. *Cell* **154**, 775-88 (2013).
54. Tesileanu, T., Colwell, L.J. & Leibler, S. Protein sectors: statistical coupling analysis versus conservation. *PLoS Comput Biol* **11**, e1004091 (2015).
55. Phillips, P.C. The language of gene interaction. *Genetics* **149**, 1167-71 (1998).
56. Breen, M.S., Kemena, C., Vlasov, P.K., Notredame, C. & Kondrashov, F.A. Epistasis as the primary factor in molecular evolution. *Nature* **490**, 535-8 (2012).
57. Starr, T.N. & Thornton, J.W. Epistasis in protein evolution. *Protein Sci* **25**, 1204-18 (2016).
58. Ortlund, E.A., Bridgham, J.T., Redinbo, M.R. & Thornton, J.W. Crystal structure of an ancient protein: evolution by conformational epistasis. *Science* **317**, 1544-8 (2007).
59. Karageorgi, M. et al. Genome editing retraces the evolution of toxin resistance in the monarch butterfly. *Nature* **574**, 409-412 (2019).
60. Phillips, P.C. Epistasis--the essential role of gene interactions in the structure and evolution of genetic systems. *Nat Rev Genet* **9**, 855-67 (2008).
61. Faure, A.J. et al. Mapping the energetic and allosteric landscapes of protein binding domains. *Nature* **604**, 175-183 (2022).
62. Park, Y., Metzger, B.P.H. & Thornton, J.W. Epistatic drift causes gradual decay of predictability in protein evolution. *Science* **376**, 823-830 (2022).
63. Ding, D. et al. Co-evolution of interacting proteins through non-contacting and non-specific mutations. *Nat Ecol Evol* **6**, 590-603 (2022).
64. Kondrashov, A.S., Sunyaev, S. & Kondrashov, F.A. Dobzhansky-Muller incompatibilities in protein evolution. *Proc Natl Acad Sci U S A* **99**, 14878-83 (2002).
65. Lunzer, M., Golding, G.B. & Dean, A.M. Pervasive cryptic epistasis in molecular evolution. *PLoS Genet* **6**, e1001162 (2010).
66. Natarajan, C. et al. Epistasis among adaptive mutations in deer mouse hemoglobin. *Science* **340**, 1324-7 (2013).
67. Doud, M.B., Ashenberg, O. & Bloom, J.D. Site-Specific Amino Acid Preferences Are Mostly Conserved in Two Closely Related Protein Homologs. *Mol Biol Evol* **32**, 2944-60 (2015).
68. Starr, T.N. et al. Shifting mutational constraints in the SARS-CoV-2 receptor-binding domain during viral evolution. *Science* **377**, 420-424 (2022).
69. Haddox, H.K., Dingens, A.S., Hilton, S.K., Overbaugh, J. & Bloom, J.D. Mapping mutational effects along the evolutionary landscape of HIV envelope. *Elife* **7**(2018).
70. Viktorovskaya, O.V. et al. Divergent contributions of conserved active site residues to transcription by eukaryotic RNA polymerases I and II. *Cell Rep* **4**, 974-84 (2013).
71. Mani, R., St Onge, R.P., Hartman, J.L.t., Giaever, G. & Roth, F.P. Defining genetic interaction. *Proc Natl Acad Sci U S A* **105**, 3461-6 (2008).
72. Qiu, C. & Kaplan, C.D. Functional assays for transcription mechanisms in high-throughput. *Methods* **159-160**, 115-123 (2019).
73. Lin, X. et al. Nested epistasis enhancer networks for robust genome regulation. *Science* **377**, 1077-1085 (2022).
74. Fowler, D.M. & Fields, S. Deep mutational scanning: a new style of protein science. *Nat Methods* **11**, 801-7 (2014).
75. Sergey Ioffe, C.S. Batch Normalization: Accelerating Deep Network Training by Reducing Internal Covariate Shift. *arXiv:1502.03167v3* (2015).
76. Hill, W.G., Goddard, M.E. & Visscher, P.M. Data and theory point to mainly additive genetic variance for complex traits. *PLoS Genet* **4**, e1000008 (2008).

849 77. Scull, C.E., Ingram, Z.M., Lucius, A.L. & Schneider, D.A. A Novel Assay for RNA
850 Polymerase I Transcription Elongation Sheds Light on the Evolutionary Divergence of
851 Eukaryotic RNA Polymerases. *Biochemistry* **58**, 2116-2124 (2019).
852 78. Duan, B., Qiu, C., Lockless, S.W., Sze, S.H. & Kaplan, C.D. Higher-order epistasis
853 within Pol II trigger loop haplotypes. *Genetics* **228**(2024).
854 79. Brueckner, F. & Cramer, P. Structural basis of transcription inhibition by alpha-amanitin
855 and implications for RNA polymerase II translocation. *Nat Struct Mol Biol* **15**, 811-8
856 (2008).
857 80. Carvalho, A.T., Fernandes, P.A. & Ramos, M.J. The Catalytic Mechanism of RNA
858 Polymerase II. *J Chem Theory Comput* **7**, 1177-88 (2011).
859 81. Huang, X. et al. RNA polymerase II trigger loop residues stabilize and position the
860 incoming nucleotide triphosphate in transcription. *Proc Natl Acad Sci U S A* **107**, 15745-
861 50 (2010).
862 82. Castro, C. et al. Nucleic acid polymerases use a general acid for nucleotidyl transfer. *Nat*
863 *Struct Mol Biol* **16**, 212-8 (2009).
864 83. Unarta, I.C., Goonetilleke, E.C., Wang, D. & Huang, X. Nucleotide addition and cleavage
865 by RNA polymerase II: Coordination of two catalytic reactions using a single active site.
866 *J Biol Chem* **299**, 102844 (2023).
867 84. Mishanina, T.V., Palo, M.Z., Nayak, D., Mooney, R.A. & Landick, R. Trigger loop of RNA
868 polymerase is a positional, not acid-base, catalyst for both transcription and
869 proofreading. *Proc Natl Acad Sci U S A* **114**, E5103-E5112 (2017).
870 85. Palo, M.Z., Zhu, J., Mishanina, T.V. & Landick, R. Conserved Trigger Loop Histidine of
871 RNA Polymerase II Functions as a Positional Catalyst Primarily through Steric Effects.
872 *Biochemistry* **60**, 3323-3336 (2021).
873 86. Araya, C.L. et al. A fundamental protein property, thermodynamic stability, revealed
874 solely from large-scale measurements of protein function. *Proc Natl Acad Sci U S A* **109**,
875 16858-63 (2012).
876 87. Melamed, D., Young, D.L., Gamble, C.E., Miller, C.R. & Fields, S. Deep mutational
877 scanning of an RRM domain of the Saccharomyces cerevisiae poly(A)-binding protein.
878 *RNA* **19**, 1537-51 (2013).
879 88. Harms, M.J. & Thornton, J.W. Analyzing protein structure and function using ancestral
880 gene reconstruction. *Curr Opin Struct Biol* **20**, 360-6 (2010).
881 89. Fowler, D.M. et al. High-resolution mapping of protein sequence-function relationships.
882 *Nat Methods* **7**, 741-6 (2010).
883 90. Toulokhonov, I., Zhang, J., Palangat, M. & Landick, R. A central role of the RNA
884 polymerase trigger loop in active-site rearrangement during transcriptional pausing. *Mol*
885 *Cell* **27**, 406-19 (2007).
886 91. Yuzenkova, Y. et al. Stepwise mechanism for transcription fidelity. *BMC Biol* **8**, 54
887 (2010).
888 92. Wang, W., Walmacq, C., Chong, J., Kashlev, M. & Wang, D. Structural basis of
889 transcriptional stalling and bypass of abasic DNA lesion by RNA polymerase II. *Proc Natl*
890 *Acad Sci U S A* **115**, E2538-E2545 (2018).
891 93. Halabi, N., Rivoire, O., Leibler, S. & Ranganathan, R. Protein sectors: evolutionary units
892 of three-dimensional structure. *Cell* **138**, 774-86 (2009).
893 94. Rivoire, O., Reynolds, K.A. & Ranganathan, R. Evolution-Based Functional
894 Decomposition of Proteins. *PLoS Comput Biol* **12**, e1004817 (2016).
895 95. Salinas, V.H. & Ranganathan, R. Coevolution-based inference of amino acid interactions
896 underlying protein function. *Elife* **7**(2018).
897 96. Cramer, P. Structure and function of RNA polymerase II. *Adv Protein Chem* **67**, 1-42
898 (2004).

899 97. Walmacq, C. et al. Rpb9 subunit controls transcription fidelity by delaying NTP
900 sequestration in RNA polymerase II. *J Biol Chem* **284**, 19601-12 (2009).
901 98. Ziegler, L.M., Khaperskyy, D.A., Ammerman, M.L. & Ponticelli, A.S. Yeast RNA
902 polymerase II lacking the Rpb9 subunit is impaired for interaction with transcription factor
903 IIF. *J Biol Chem* **278**, 48950-6 (2003).
904 99. Nouraini, S., Archambault, J. & Friesen, J.D. Rpo26p, a subunit common to yeast RNA
905 polymerases, is essential for the assembly of RNA polymerases I and II and for the
906 stability of the largest subunits of these enzymes. *Mol Cell Biol* **16**, 5985-96 (1996).
907 100. Cramer, P. Organization and regulation of gene transcription. *Nature* **573**, 45-54 (2019).
908 101. Schier, A.C. & Taatjes, D.J. Structure and mechanism of the RNA polymerase II
909 transcription machinery. *Genes Dev* **34**, 465-488 (2020).
910 102. Vos, S.M., Farnung, L., Linden, A., Urlaub, H. & Cramer, P. Structure of complete Pol II-
911 DSIF-PAF-SPT6 transcription complex reveals RTF1 allosteric activation. *Nat Struct Mol*
912 *Biol* **27**, 668-677 (2020).
913 103. Castro, C. et al. Two proton transfers in the transition state for nucleotidyl transfer
914 catalyzed by RNA- and DNA-dependent RNA and DNA polymerases. *Proc Natl Acad Sci*
915 *U S A* **104**, 4267-72 (2007).
916 104. Gregory, M.T., Gao, Y., Cui, Q. & Yang, W. Multiple deprotonation paths of the
917 nucleophile 3'-OH in the DNA synthesis reaction. *Proc Natl Acad Sci U S A* **118**(2021).
918 105. Belogurov, G.A. & Artsimovitch, I. The Mechanisms of Substrate Selection, Catalysis,
919 and Translocation by the Elongating RNA Polymerase. *J Mol Biol* **431**, 3975-4006
920 (2019).
921 106. Jenks, M.H., O'Rourke, T.W. & Reines, D. Properties of an intergenic terminator and
922 start site switch that regulate IMD2 transcription in yeast. *Mol Cell Biol* **28**, 3883-93
923 (2008).
924 107. Kuehner, J.N. & Brow, D.A. Regulation of a eukaryotic gene by GTP-dependent start site
925 selection and transcription attenuation. *Mol Cell* **31**, 201-11 (2008).
926 108. Malik, I., Qiu, C., Snavely, T. & Kaplan, C.D. Wide-ranging and unexpected
927 consequences of altered Pol II catalytic activity in vivo. *Nucleic Acids Research* **45**,
928 4431-4451 (2017).
929 109. Qiu, C. et al. Thiolutin has complex effects in vivo but is a direct inhibitor of RNA
930 polymerase II in vitro. *Nucleic Acids Res* **52**, 2546-2564 (2024).
931 110. Greger, I.H. & Proudfoot, N.J. Poly(A) signals control both transcriptional termination and
932 initiation between the tandem GAL10 and GAL7 genes of Saccharomyces cerevisiae.
933 *Embo J* **17**, 4771-9 (1998).
934 111. Kaplan, C.D., Holland, M.J. & Winston, F. Interaction between transcription elongation
935 factors and mRNA 3'-end formation at the Saccharomyces cerevisiae GAL10-GAL7
936 locus. *J Biol Chem* **280**, 913-22 (2005).
937 112. Simchen, G., Winston, F., Styles, C.A. & Fink, G.R. Ty-mediated gene expression of the
938 LYS2 and HIS4 genes of Saccharomyces cerevisiae is controlled by the same SPT
939 genes. *Proc Natl Acad Sci U S A* **81**, 2431-4 (1984).
940 113. Aguilera, A. Formamide sensitivity: a novel conditional phenotype in yeast. *Genetics*
941 **136**, 87-91 (1994).
942 114. Sing-Hoi Sze, C.D.K. Codon-Based Sequence Alignment for Mutation Analysis by High-
943 Throughput Sequencing. in *2018 IEEE 8th International Conference on Computational*
944 *Advances in Bio and Medical Sciences (ICCABS)* (2018).
945 115. Notredame, C., Higgins, D.G. & Heringa, J. T-Coffee: A novel method for fast and
946 accurate multiple sequence alignment. *J Mol Biol* **302**, 205-17 (2000).
947 116. Price, M.N., Dehal, P.S. & Arkin, A.P. FastTree 2--approximately maximum-likelihood
948 trees for large alignments. *PLoS One* **5**, e9490 (2010).

FIGURES/LEGENDS

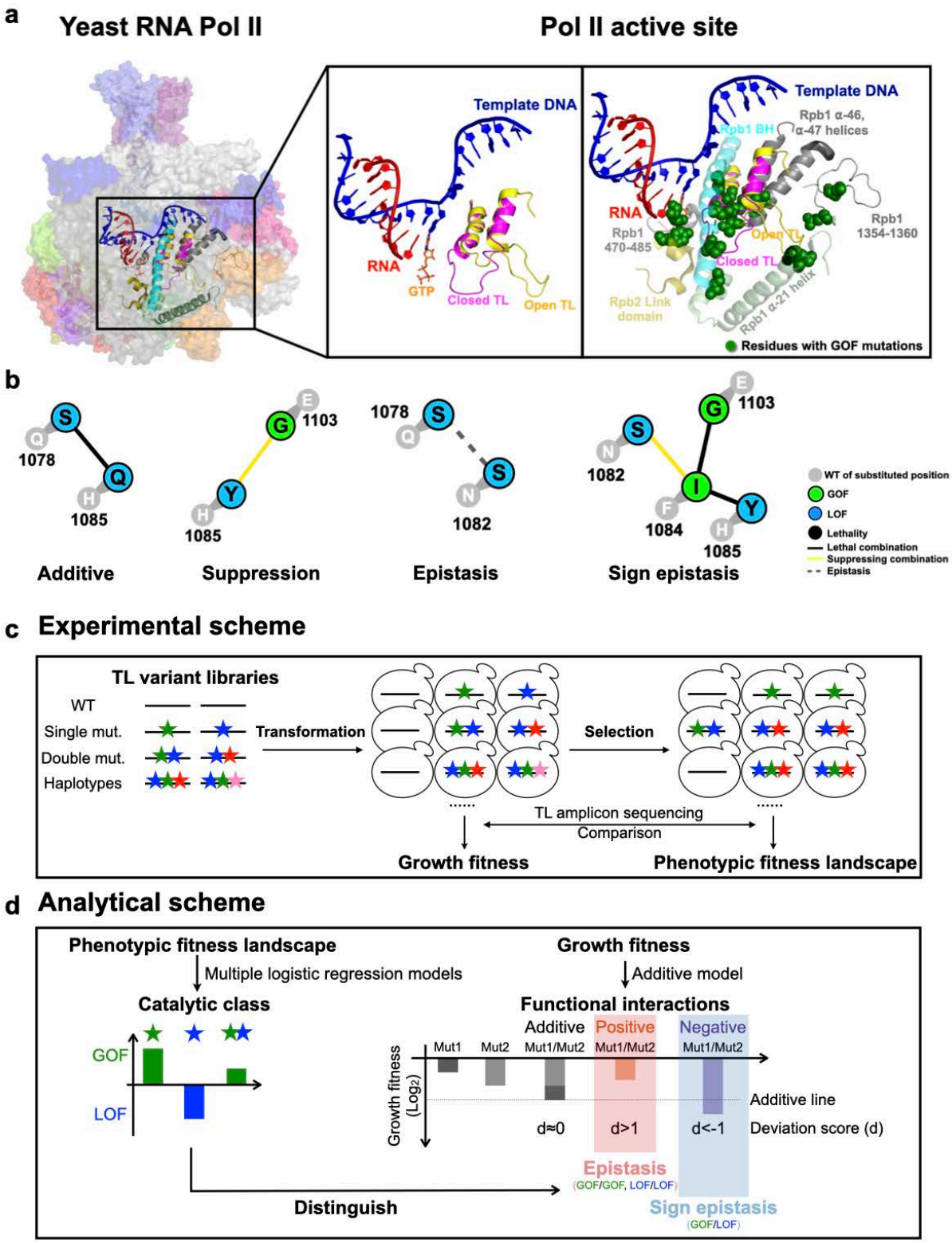

Figure 1. Schematics of the Pol II active site interaction landscape. a. The Pol II active site is embedded in the center of a 12-subunit complex (left panel). Pol II functions are supported by distinct TL conformational states. An open TL (PDB: 5C4X)[42] and closed TL (PDB: 2E2H)[12] conformations are shown in the middle panel. GOF mutations have been identified in the TL and

its proximal domains (right panel), suggesting TL mobility and function may be impacted by adjacent residues. **b.** Examples of inter-residue genetic interactions. WT residues are shown in grey circles with number indicating residue position in Rpb1. Mutant substitutions are shown in colored circles, with color representing mutant class. Colored lines between mutant substitutions represent types of genetic interactions. **c.** Overview of experimental approach. We synthesized 10 libraries of TL variants represented by colored stars. Libraries were transformed into WT or mutated yeast strains. A selection assay was subsequently performed by scraping and replating the transformants onto different media for phenotyping. DNA was extracted from yeast from all conditions, and went through TL region amplification, and Illumina sequencing. Read counts for variants on general conditions were used to determine growth fitness, while read counts on other conditions were used to determine the phenotypic fitness landscape (see **Methods**). **d.** Overview of analytical approach for determining interaction landscape. Mutant conditional growth fitnesses were calculated using allele frequencies under selective growth conditions and subjected to two logistic regression models for classification/prediction of catalytic defects. Double mutant interactions were computed using growth fitness. Classification allowed epistatic interactions to be deduced from double mutant growth fitness (see **Methods**).

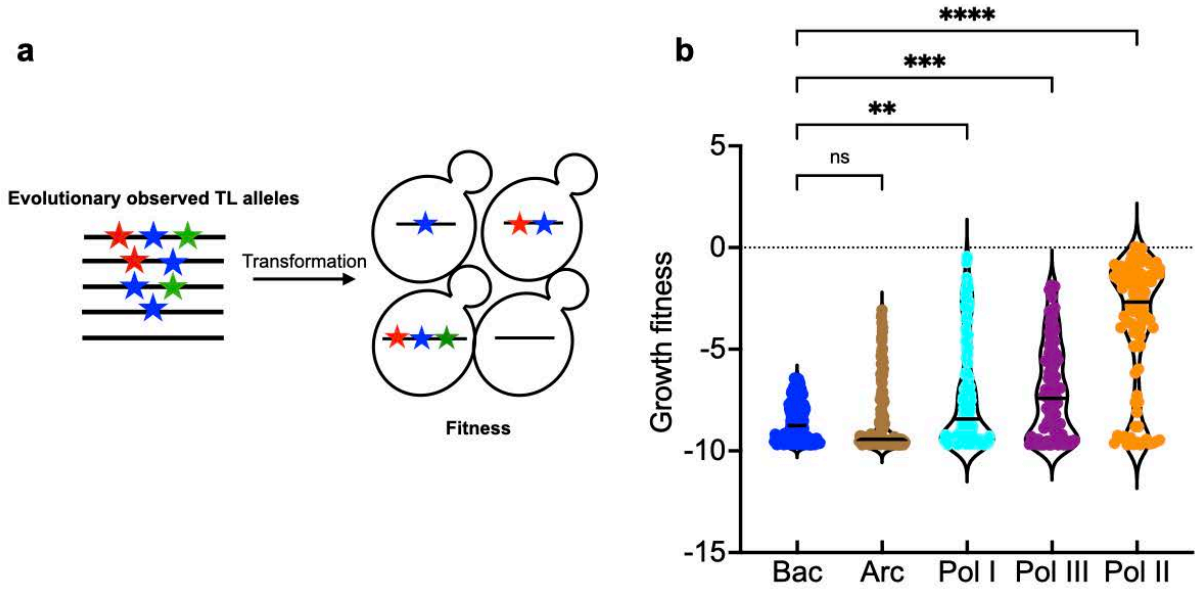

Figure 2. Contextual epistasis shapes TL evolution. a. Schematic for the TL evolutionary haplotypes library. We selected 662 TL haplotypes representing TL alleles from bacterial, archaeal and the three conserved eukaryotic msRNAPs. These TL alleles were transformed into yeast and were phenotyped under selective conditions. **b.** Fitness of evolutionarily observed TL haplotypes in the yeast Pol II background. The Pol II WT TL fitness (0) is labeled as dotted line. Kruskal-Wallis test was performed for comparison and significant levels ($P < 0.05$) were labeled.

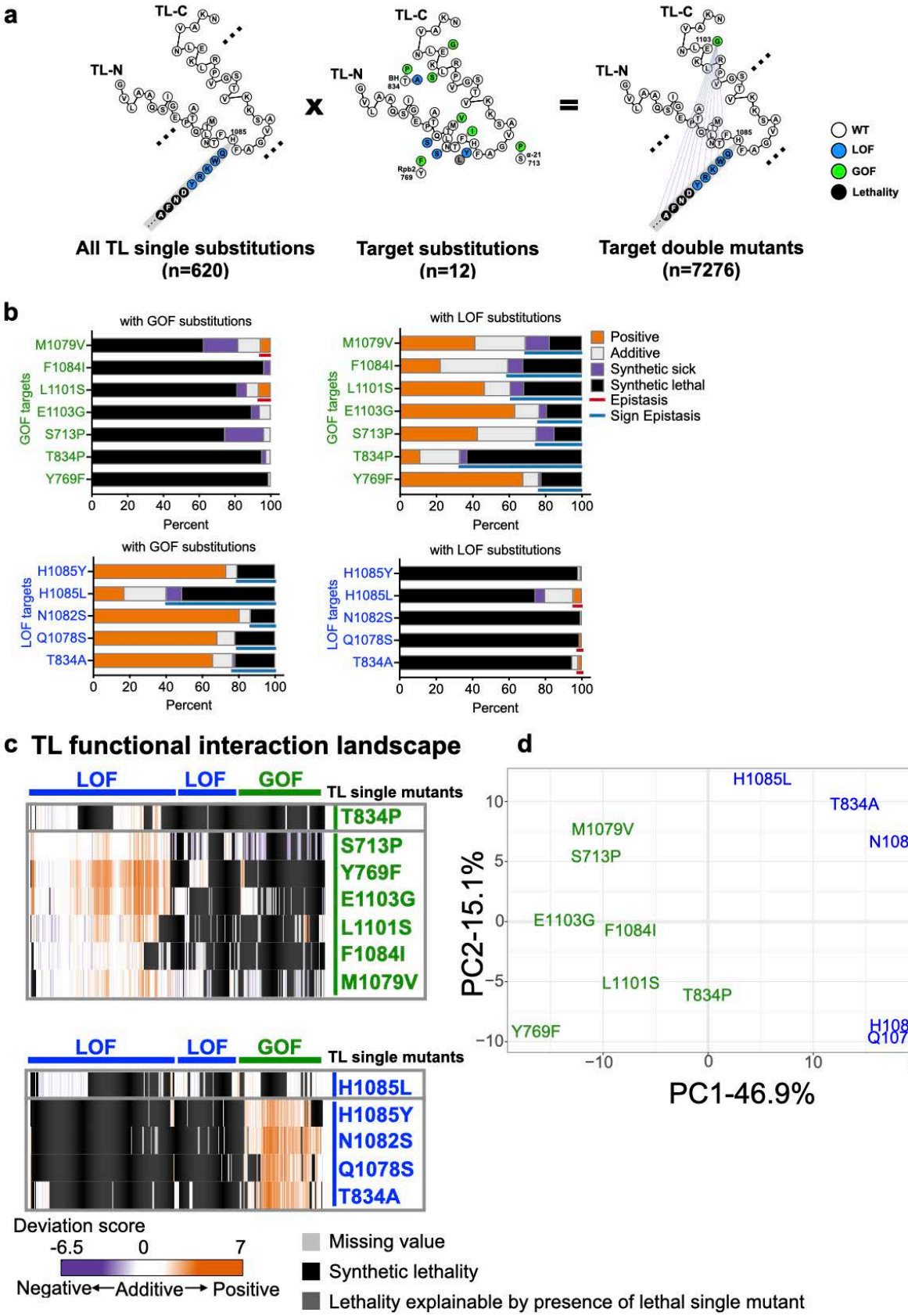
a
TL-C
TL-N
All TL single substitutions
(n=620)
Target substitutions
(n=12)
Target double mutants
(n=7276)
WT
LOF
GOF
Lethality
b
with GOF substitutions
with LOF substitutions
GOF targets
M1079V
F1084I
L1101S
E1103G
S713P
T834P
Y769F
LOF targets
H1085Y
H1085L
N1082S
Q1078S
T834A
Percent
Positive
Additive
Synthetic sick
Synthetic lethal
Epistasis
Sign Epistasis
c TL functional interaction landscape
LOF
GOF
TL single mutants
Deviation score
-6.5
0
7
Negative←Additive→Positive
Missing value
Synthetic lethality
Lethality explainable by presence of lethal single mutant
d
PC2-15.1%
PC1-46.9%

991 **Figure 3. Pol II TL interaction landscape distinguishes mutants with similar phenotypes.**
992 **a.** Design of the targeted double mutant libraries. All possible substitutions at each TL residue
993 (represented with a simplified format in the left panel) and twelve "probe" mutations (eight within
994 the TL and four in TL-proximal domains) (middle panel) were combined with to generate 7280
995 double mutants (right panel). 7276 mutants passed the reproducibility filter and were used for
996 interaction analyses. **b.** The percentage of functional interactions observed for each probe
997 mutant with viable GOF or LOF TL substitutions. Epistasis and sign epistasis are labeled with
998 colored lines. **c.** Pol II-TL functional interaction landscape with interactions represented by
999 deviation scores. The upper panel shows interactions of GOF probe mutants in combination of
1000 viable GOF or LOF TL substitutions. The lower panel shows interactions of combinations with
1001 LOF probe mutants. **d**. Principal component analysis (PCA) of deviation scores across double
1002 mutant interactions for 12 probe mutants (see **Methods**).

1003

1004

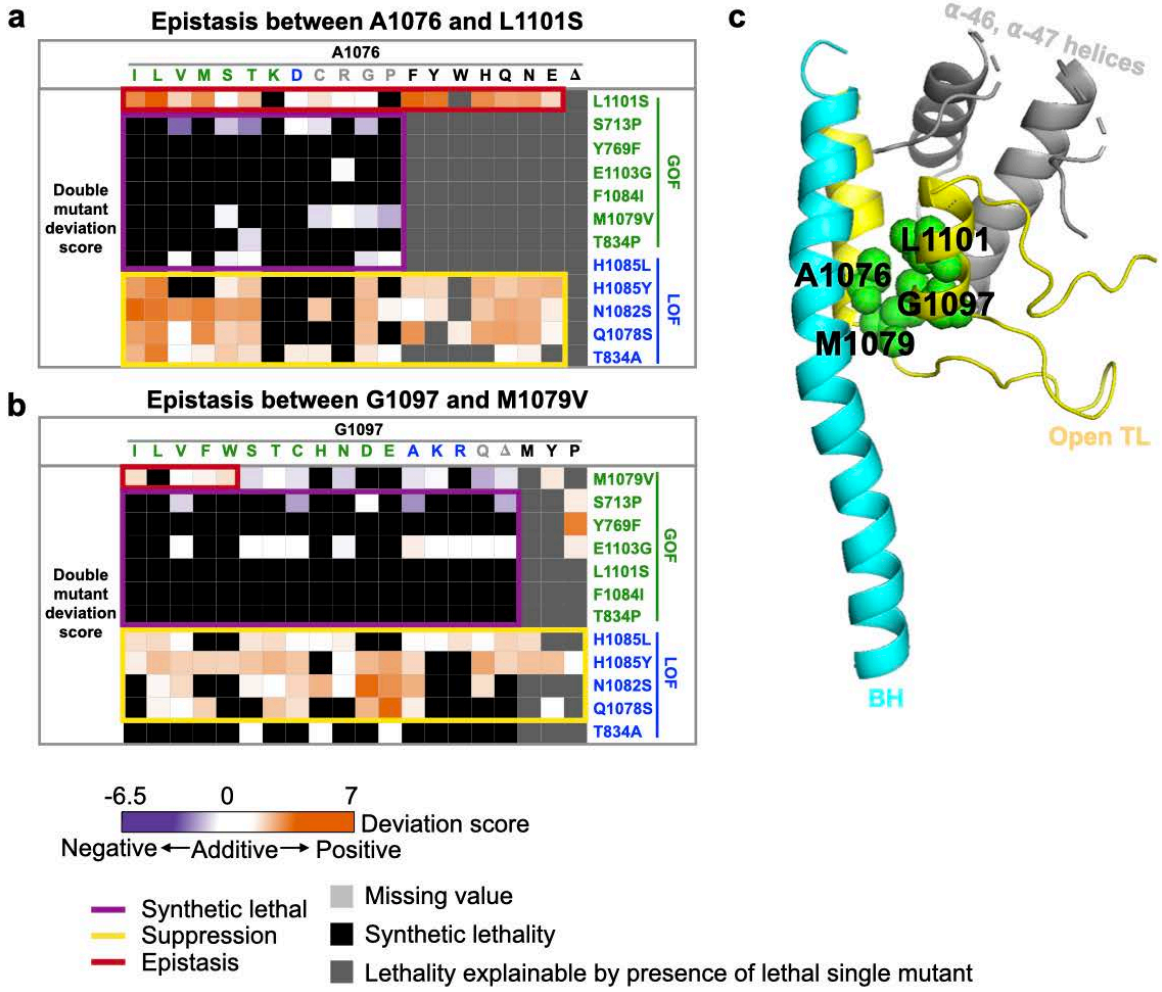

Figure 4. Pol II TL interaction landscape reveals functional dependency of proximal residues. a-b. Specific epistatic interactions observed between hydrophobic residues A1076 and L1101 (A), and M1079 and G1097 are shown as heatmaps (B). The x-axis of both heatmaps are 20 substitutions ordered by predicted phenotypic classes, and the color of substitution represents the phenotypic class of the substitution. GOF substitution is in green, LOF is in blue, unclassified is in gray, and lethal (fitness < -6.5) is in black. **c.** The epistatic interactions we identified between A1076 and L1101, together with M1079 and G1097 are shown on the five-helix bundle of Pol II active site (PDB: 5C4X)[42].

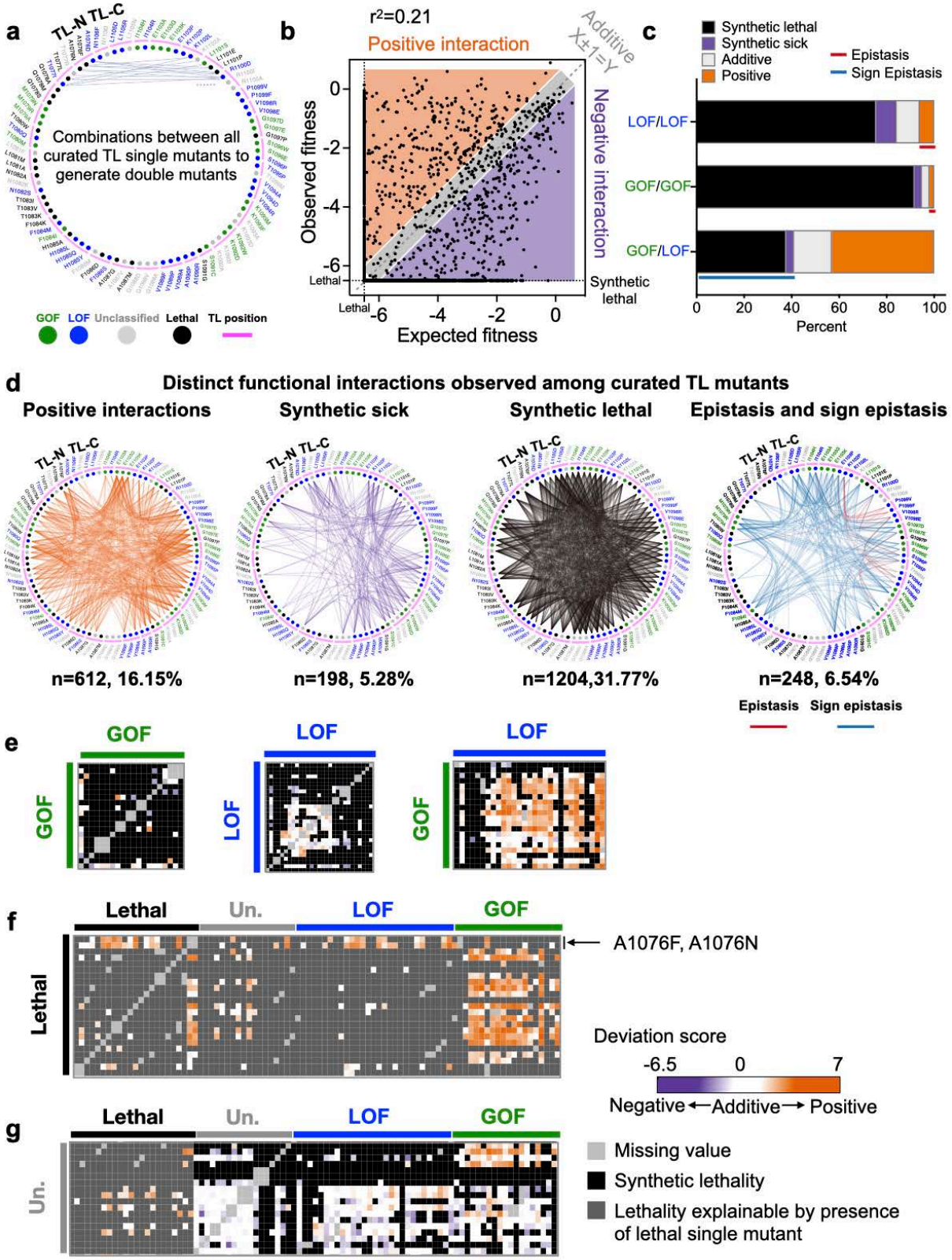

Figure 5. Widespread epistasis in the Pol II TL interaction landscape. a. Design of the pairwise double mutant library. We curated 2-4 substitutions for each TL residue (in total 90 substitutions, n(GOF) = 18, n(LOF) = 30, n(Unclassified) = 19, n(Lethal) = 23), and combined

them with each other to generate double mutants. 3910 double mutants representing combinations between any two TL residues were measured and 3790 of them passed the reproducibility filter. WT TL residue positions are indicated with magenta arch. Phenotype classes of single substitutions are shown as colored circles (GOF in green, LOF in blue) while unclassified mutants are in grey and lethal mutants are in black. **b.** An xy-plot of observed double mutant growth fitness measured in our experiment (Y-axis) and expected fitness from the addition of two constituent single mutants' fitnesses (X-axis). N (positive) = 612. N (Negative) = 1402. N (Additive) = 1776. N (Sum)=3790. Lethal threshold (-6.5) is labeled with dotted lines on X and Y axis. The additive line where $X \pm 1 = Y$ is indicated with dashed line. Simple linear regression was performed, and the best fit equation is $Y = 0.52X - 2.55$, $r^2 = 0.21$, $P < 0.0001$. **c.** Percent of interactions observed from each combination group. N (LOF/LOF) = 412. N (GOF/GOF) = 156. N (GOF/LOF) = 534. Epistasis and sign epistasis are indicated with colored lines. **d.** Various groups of interactions are displayed in a network format for clarity. In these networks, the TL structure is simplified to a circle, with the TL-N terminal and C-terminal of the TL connected. WT TL residues are represented by magenta arches, and selected substitutions are labeled beside these arches. The color of the label represents the phenotype of each substitution. A colored line connects two substitutions if there is interaction between them, with the line color representing the interaction type. For example, in the “Epistasis and sign epistasis” network, we selected three substitutions at K1102: K1102P, K1102L and K1102A. They show epistasis with V1094D and R, T1095P, S1096P, V1098R and P1099F and V. These interactions are labeled with red lines. The observed epistasis, indicated by red lines, accumulated at the TL-C terminal, indicating a functional dependency in this region. **e-g.** The intra-TL functional interaction heatmaps of various combinations. Double mutant deviation scores are shown in the heatmap. Annotations at the top and left indicate the curated single mutants and their predicted phenotypic classes from multiple logistic regression modeling. GOF/GOF, LOF/LOF, and GOF/LOF combinations are shown in **e**. Combinations with lethal single substitutions are in F. Combinations with unclassified mutants are in **g**.

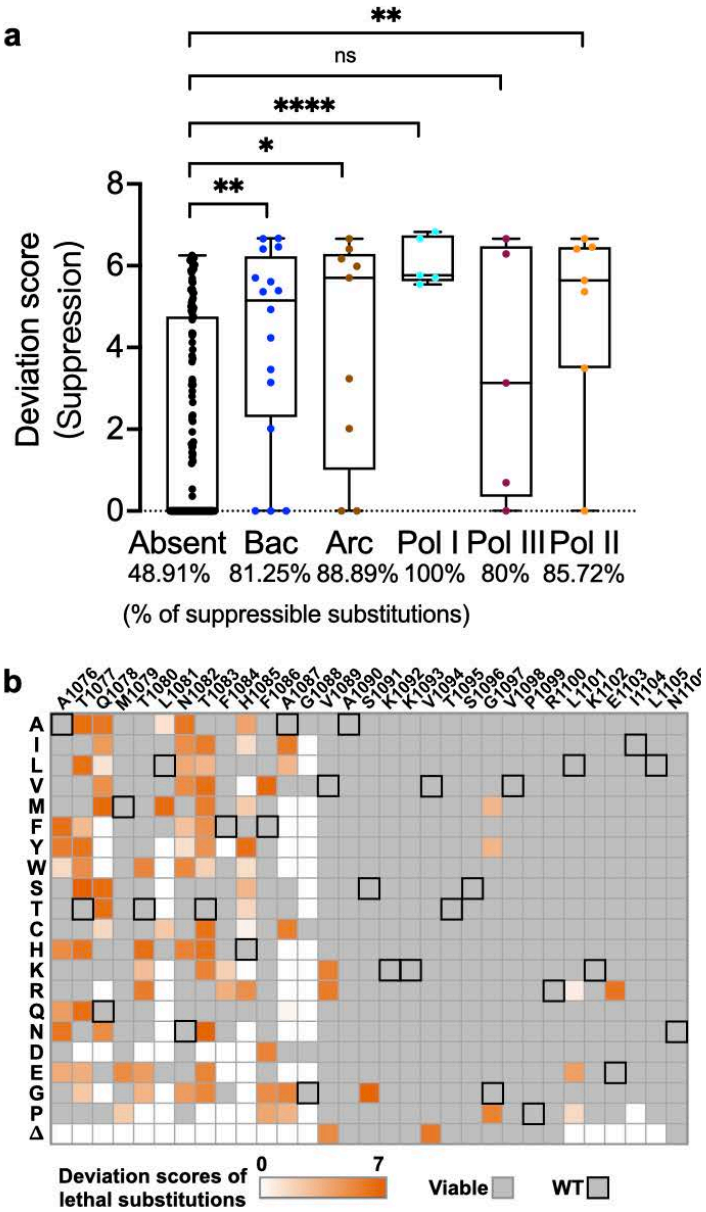

Figure 6. Contextual epistasis shapes TL evolution. a. A comparison of the maximum deviation score of each TL lethal single substitution that is present in any evolutionary TL haplotypes from bacterial, archaeal or eukaryotic Pols versus those that have not been observed in any species. The evolutionary TL haplotypes were from multiple sequence alignments (MSA). 9 substitutions were found in an MSA of 542 archaeal TL sequences that are lethal when present in yeast as a single substitution. 17 were found in an MSA of 1403 bacterial TLs, 5 were found in 749 Pol I TLs, 7 were found in 499 Pol II TLs, and 5 were found in 539 Pol III TLs. Evolutionarily observed lethal substitutions were compared to those unobserved in our TL MSA. The percentage of total suppressible lethal single mutants for each group is labeled at the bottom of the plot. Boxes are: center line, median; box limits, second and third quartiles; whiskers, maximum and minimum points. Statistical comparison was done with the Mann-Whitney test and the significant levels ($P < 0.05$) are shown in the figure. **b.** A heatmap displays the highest deviation scores of lethal single substitutions. The x-axis represents the wild-type residues and positions of the yeast Pol II TL, while the y-axis shows 20 substitutions. Viable

substitutions are marked with gray boxes, and wild-type amino acids are indicated with gray boxes with black edge. The highest deviation scores of lethal substitutions are shown in colored boxes, ranging from white to orange, reflecting the strength of suppression.

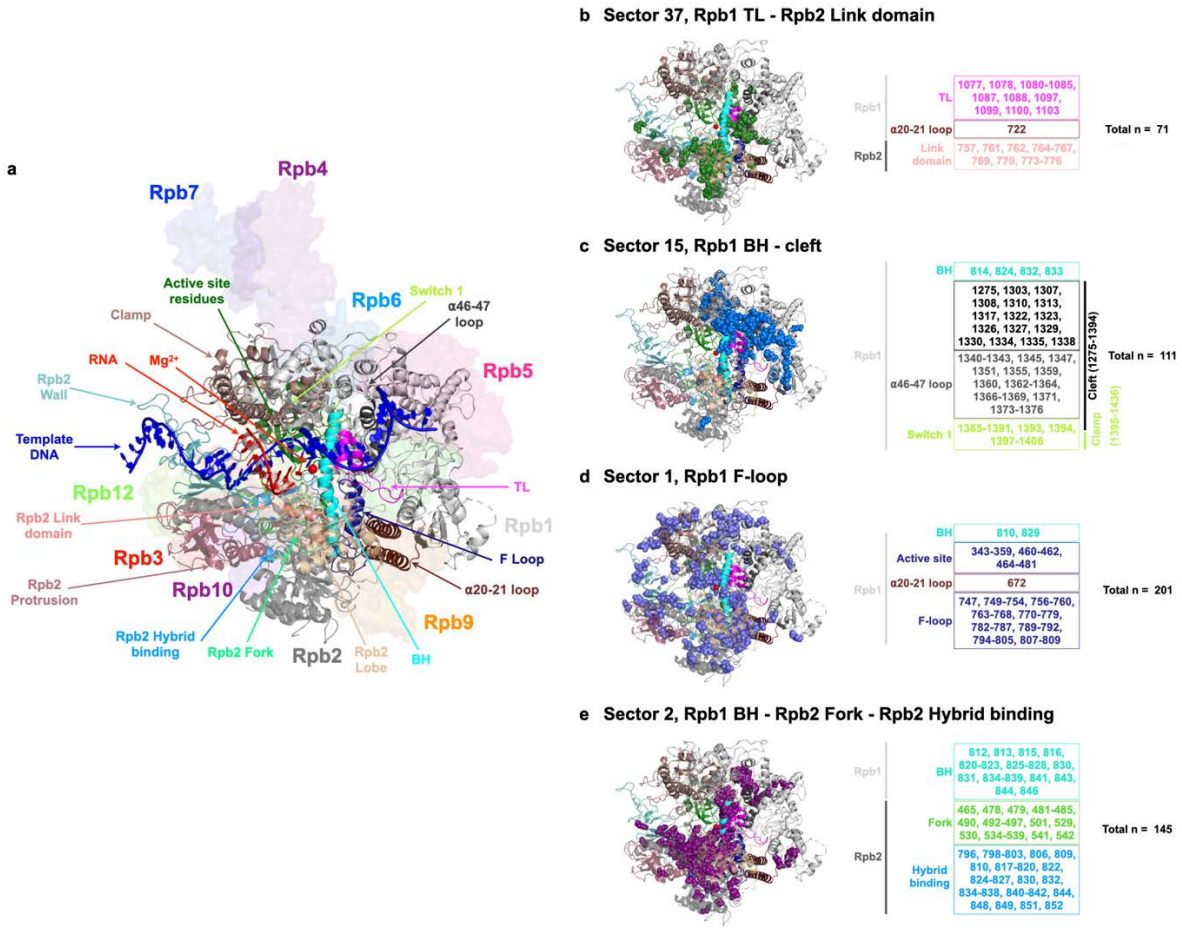

Figure 7. Ultra-conserved TL co-evolves with Pol II residues through diverse pathways. a. Structure representations of Pol II active site. Pol II subunits are showed with surface in different colors**.** The active site domains are in cartoon format. Rpb1 active site residues 346-375 and 436-508. Rpb1 TL, 1076-1106. Rpb1 BH, 810-846. Rpb1 α20-21 loop, 672-737. Rpb1 F loop, 747-810. Rpb1 α46-47 loop, 1339-1378. Rpb1 switch 1, 1385-1407. Rpb1 clamp, 1-95, 235-346, and 1395-1436. Rpb2 link domain, 757-776. Rpb2 Fork, 465-547. Rpb2 hybrid binding, 750-852. Rpb2 wall, 852-973. Rpb2 protrusion, 44-218. Rpb2 lobe, 218-405. **b-e**. Four major coevolution sectors of Pol II active site residues were identified through statistical coupling analysis. The residues within each active site domain and the total number of residues in each sector are labeled. These sectors are mapped on the yeast Pol II Rpb1/Rpb2 structure (PDB: 5C4X)[42].

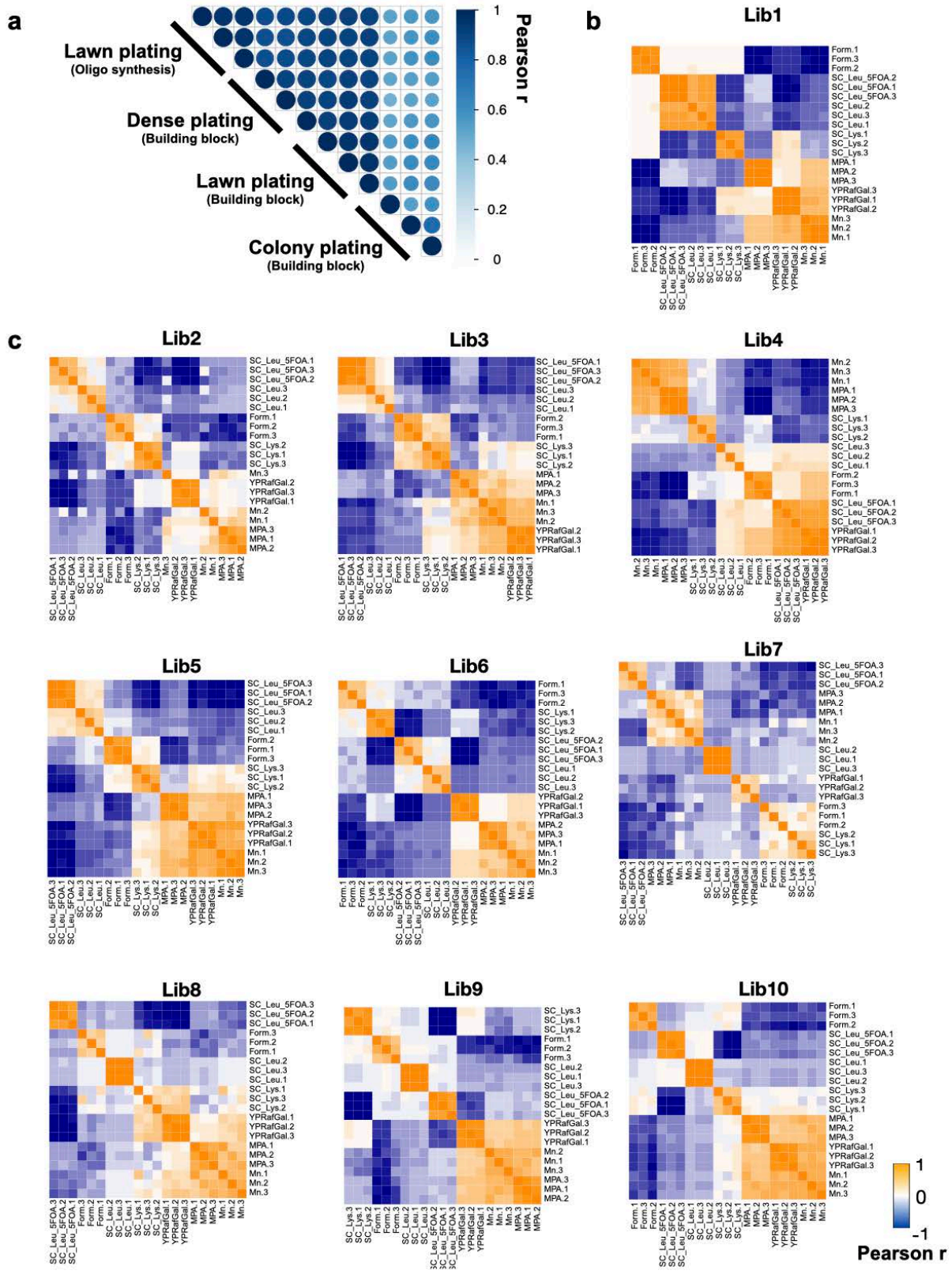

Extended Data Fig.1 Pol II deep mutational scanning is highly reproducible. a. Single mutant growth fitness from mutants in libraries constructed from synthesized oligos correlated

1083 well with our previous library constructed by a random building block approach when plating
1084 conditions were the same. Qiu *et al*[17] plated at a lower density (colony plating) that we
1085 speculated added noise to the analysis. When plating densely ("dense" and "lawn" conditions)
1086 our new and old libraries showed highly reproducible fitness determinations for single mutants.
1087 **b-c.** Biological replicates for each library showed high reproducibility for all conditions. Pearson
1088 correlation of each library was calculated with three replicates for viable mutant fitness on all
1089 selective conditions.

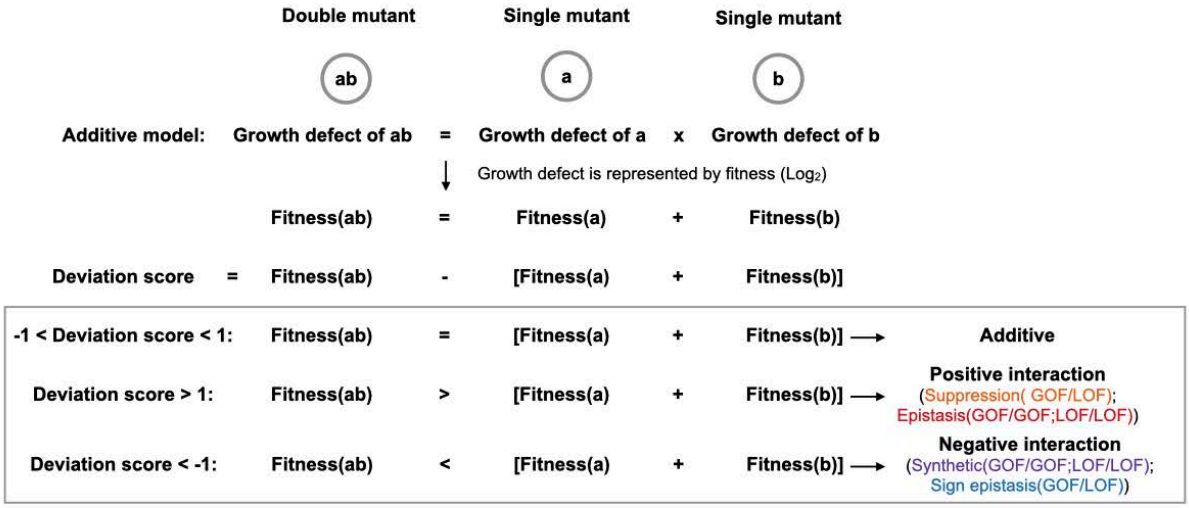

Extended Data Fig.2 Detection of functional interactions by deviation score. For a pseudo double mutant *ab*, the difference between its observed fitness (*ab*) and expected fitness (*ab*) adding the fitness of two constituent single mutants (*a* and *b*) determines the type of interaction between the two mutants. Positive or negative interactions are determined if the deviation score is greater than 1 or smaller than –1. Specific epistatic interactions are further distinguished from general suppression or synthetic sick or lethal interactions using predicted mutant catalytic defect classes (GOF or LOF).

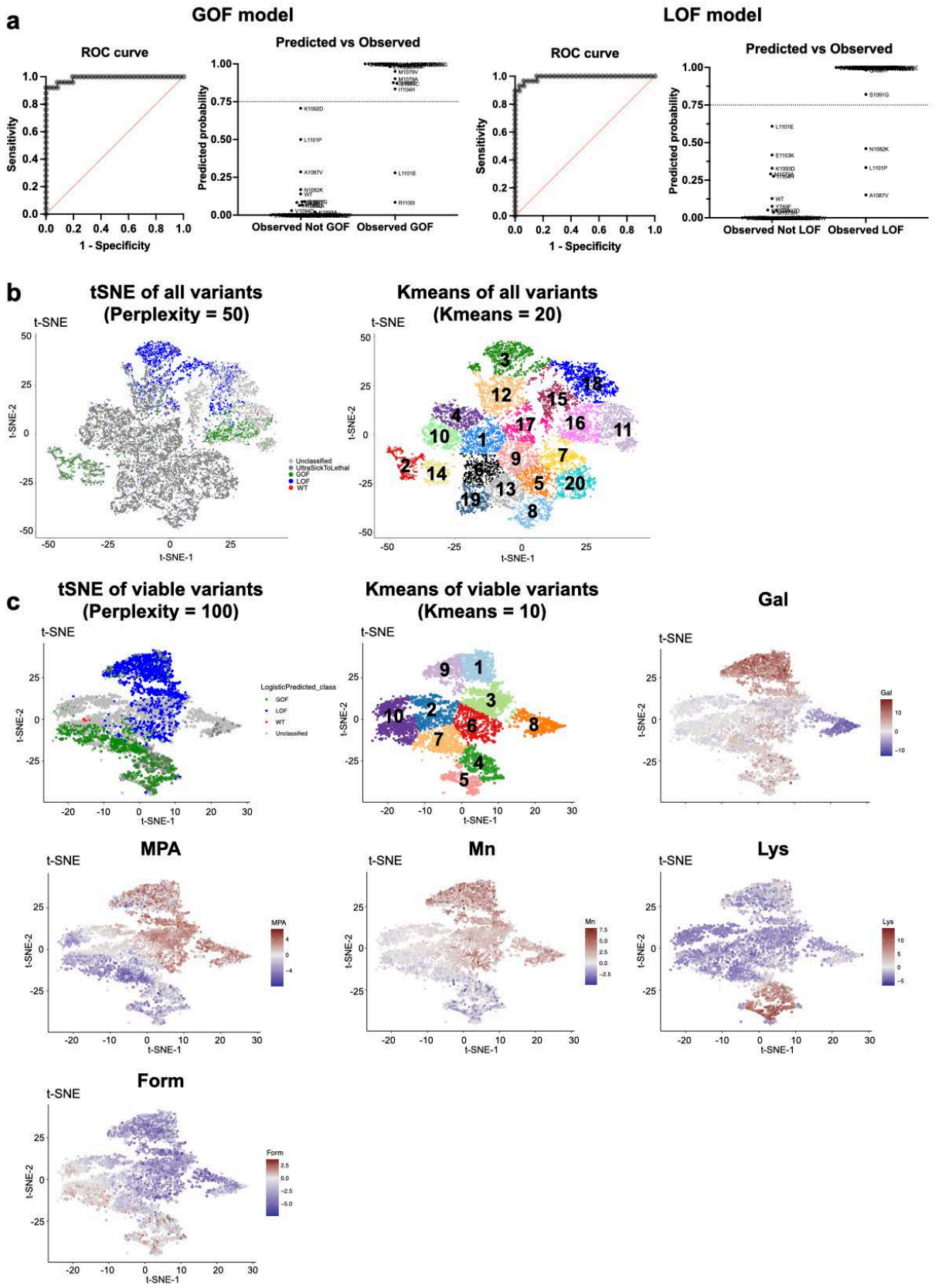
a
GOF model
ROC curve
Sensitivity
1 - Specificity
Predicted vs Observed
Predicted probability
Observed Not GOF
Observed GOF
LOF model
ROC curve
Sensitivity
1 - Specificity
Predicted vs Observed
Predicted probability
Observed Not LOF
Observed LOF
b
tSNE of all variants
(Perplexity = 50)
t-SNE
t-SNE-1
t-SNE-2
Unclassified
UltraSickToLethal
GOF
LOF
WT
Kmeans of all variants
(Kmeans = 20)
c
tSNE of viable variants
(Perplexity = 100)
LogisticPredicted_class
GOF
LOF
WT
Unclassified
Kmeans of viable variants
(Kmeans = 10)
Gal
MPA
Mn
Lys
Form

1100

Extended Data Fig.3 Classification of mutant catalytic defects with machine learning algorithms. a. ROC curves for two multiple logistic regression models used to determine mutant catalytic class. Using 65 mutants with validated in vitro determined catalytic defects and conditional growth fitness measured in our experiment, we trained two models to classify variants as GOF or LOF. The GOF AUROC is 0.9889 ($P \leq 0.0001$), whereas the LOF ROC is 0.9914 ($P \leq 0.0001$). The predicted vs. observed graphs display the predicted probability of 65 known mutants would be GOF or LOF. The threshold we used to determine GOF or LOF mutations is shown by lines at 0.75. Details of the models are in Supplemental Table 6. **b.** Left: t-SNE projection of all mutants (n=15174) with perplexity = 50. Right: k-means cluster of all mutants with 20 clusters. The t-SNE and k-means projections suggest GOF are in 3 clusters (cluster 2, 14, and 16), LOF are in 2 clusters (cluster 3 and 18), and unclassified mutants are in 2 clusters (11 and 15). Most ultra-sick/lethal mutants (fitness <= -6.5) are projected together into 13 clusters, likely due to significant noise from low read counts across conditions. **c.** Feature plot of viable mutations in t-SNE and k-means projections (n=6054). Ultra-sick/lethal mutations were removed and the viable mutants were projected with t-SNE (perplexity = 100) and K-means (10 clusters). GOF were grouped into 4 clusters (4, 5, 7 and 10) and LOF were in 4 clusters (1, 3, 6, and 9). Each spot in the projection represents a mutant and it is colored based on the fitness of the mutant in selective conditions. GOF and LOF mutants in different clusters are related to various phenotype patterns. GOF clusters 7 and 10 are defined by strong MPA^S, while clusters 4 and 5 show slight MPA^S, Gal^R, Mn^S, but strong Lys^+. Slight $Form^S$ is a common feature across four GOF clusters. LOF clusters 3 and 6 show slight Mn^R, while clusters 1 and 9 are strongly Mn^R and Gal^R. There are three common features in all LOF clusters: MPA^R, $Form^S$, and Lys^-. Cluster 8, which mostly contain unclassified mutants, appear defined by Gal super sensitivity, indicating a potential specific defect defining this cluster.

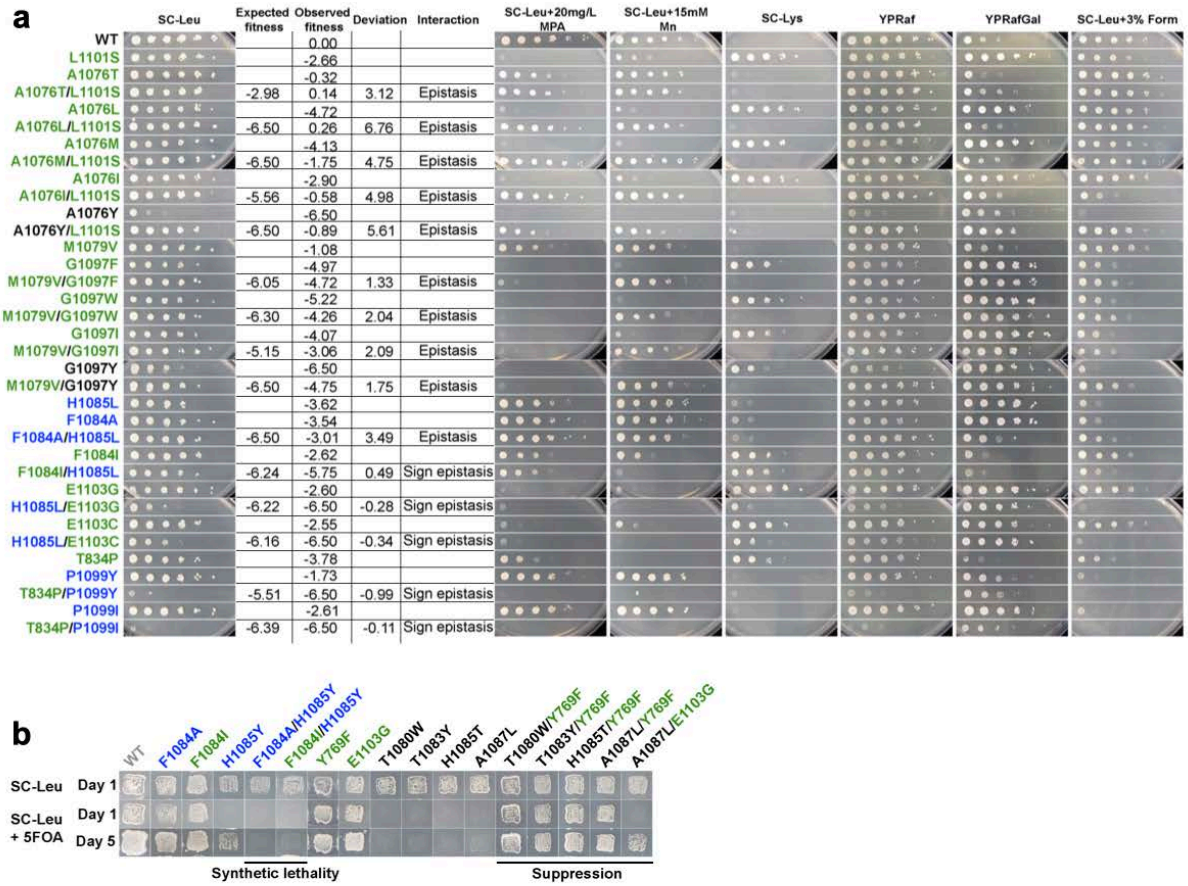

	Expected fitness	Observed fitness	Deviation	Interaction
WT		0.00		
L1101S		-2.66		
A1076T		-0.32		
A1076T/L1101S	-2.98	0.14	3.12	Epistasis
A1076L		-4.72		
A1076L/L1101S	-6.50	0.26	6.76	Epistasis
A1076M		-4.13		
A1076M/L1101S	-6.50	-1.75	4.75	Epistasis
A1076I		-2.90		
A1076I/L1101S	-5.56	-0.58	4.98	Epistasis
A1076Y		-6.50		
A1076Y/L1101S	-6.50	-0.89	5.61	Epistasis
M1079V		-1.08		
G1097F		-4.97		
M1079V/G1097F	-6.05	-4.72	1.33	Epistasis
G1097W		-5.22		
M1079V/G1097W	-6.30	-4.26	2.04	Epistasis
G1097I		-4.07		
M1079V/G1097I	-5.15	-3.06	2.09	Epistasis
G1097Y		-6.50		
M1079V/G1097Y	-6.50	-4.75	1.75	Epistasis
H1085L		-3.62		
F1084A		-3.54		
F1084A/H1085L	-6.50	-3.01	3.49	Epistasis
F1084I		-2.62		
F1084I/H1085L	-6.24	-5.75	0.49	Sign epistasis
E1103G		-2.60		
H1085L/E1103G	-6.22	-6.50	-0.28	Sign epistasis
E1103C		-2.55		
H1085L/E1103C	-6.16	-6.50	-0.34	Sign epistasis
T834P		-3.78		
P1099Y		-1.73		
T834P/P1099Y	-5.51	-6.50	-0.99	Sign epistasis
P1099I		-2.61		
T834P/P1099I	-6.39	-6.50	-0.11	Sign epistasis

Extended Data Fig.4 Genetic interactions detected with spot assay and patch assay are consistent with high-throughput results. To verify the genetic interactions observed in high throughput experiment, we picked 63 mutants to measure the genetic interactions with spot assay (**a**) or patch assay (**b**). They are consistent. The fitness, deviation scores and corresponding genetic interactions measured in high throughput experiment are indicated in **a**. The names of GOF mutants are labeled with green color, LOF mutants are labeled with blue, ultra-sick to lethal mutants are labeled with black color.

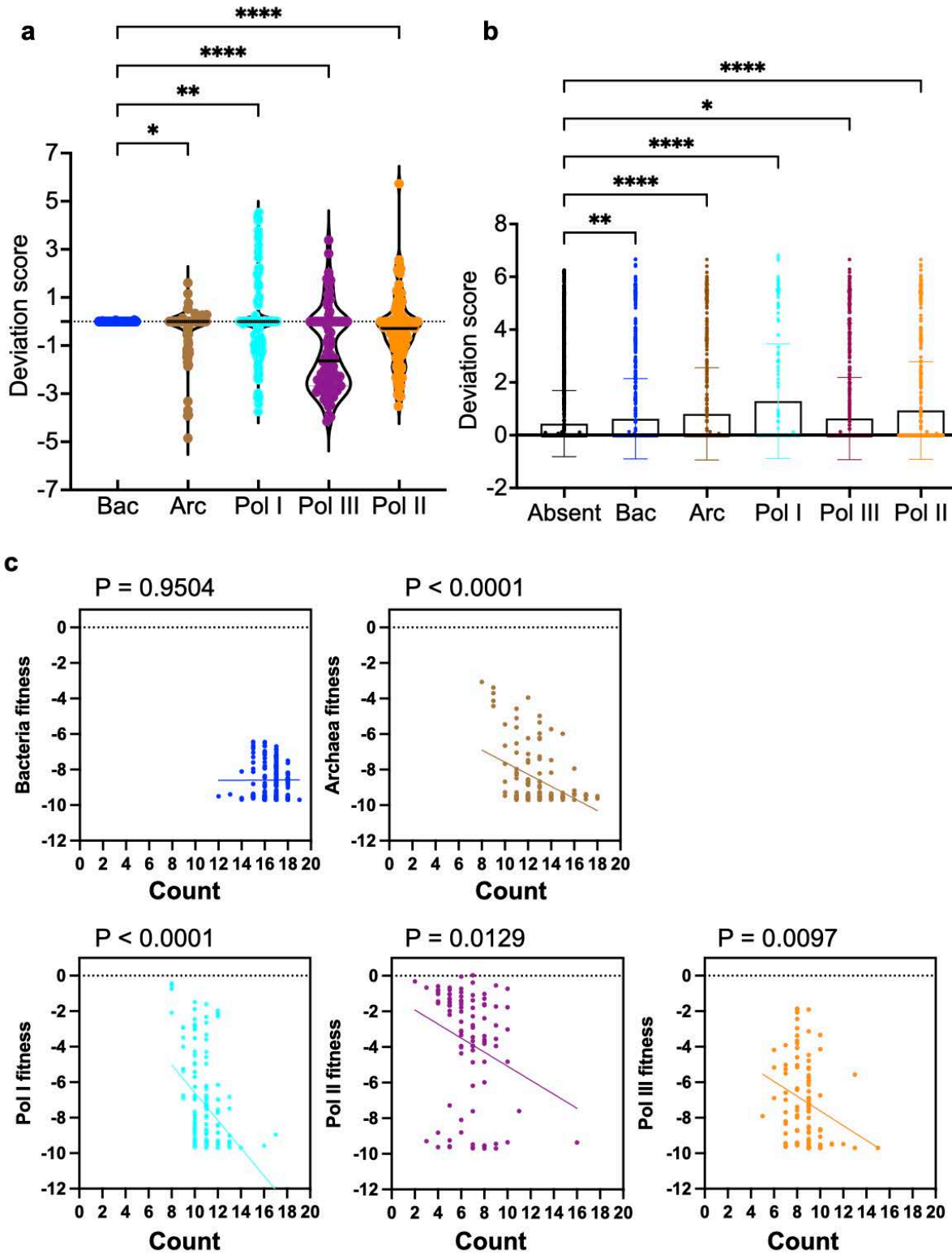

Extended Data Fig.5 Contextual epistasis affects fitness of TL haplotypes. a. Distributions of deviation scores of the TL haplotypes in each group. **b.** Comparison of the mean deviation scores of lethal single substitutions that are present in different species and those that are

absent in any species. Standard deviation values are also shown in the bar plot. ANOVA multiple comparison was applied to compare the mean deviation score of the “Absent” group to each of the other groups and significant levels ($P < 0.05$) are shown in the figure. **c.** An xy-plot of evolutionary observed TL haplotypes fitness versus the numbers of substitutions in the haplotypes. Simple linear regression was performed for each plot. Bacteria fitness vs count: $Y = 0.004267*X – 8.660$, $r^2=2.152e-005$. Archaea fitness vs count: $Y = -0.3406*X - 4.175$, $r^2=0.1568$. Pol I fitness vs count: $Y = -0.7818*X + 1.235$, $r^2=0.1521$. Pol II fitness vs count: $Y = -0.3943*X – 1.132$, $r^2=0.06535$. Pol III fitness vs count: $Y = -0.4148*X – 3.468$, $r^2=0.06984$. The P values of the slopes are labeled.

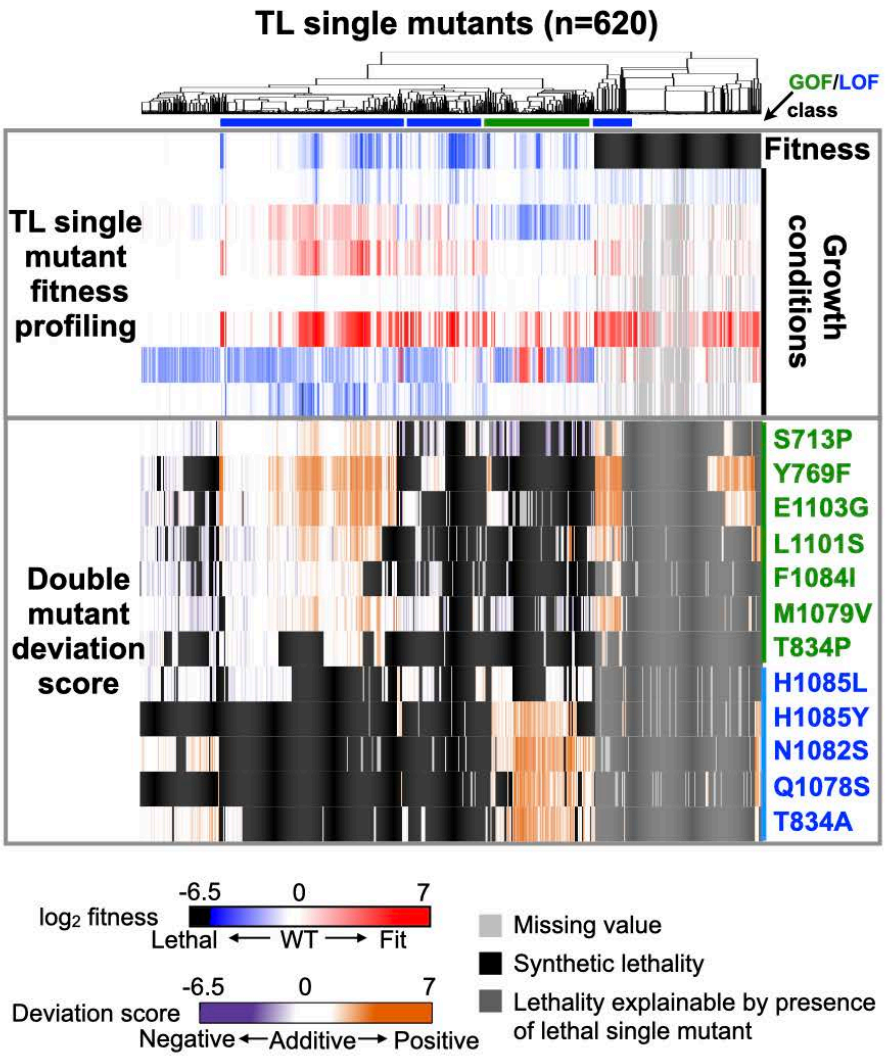

Extended Data Fig.6 The functional interaction landscape of probe mutants. The functional interaction landscape is shown as a heatmap. The upper part of the heatmap shows all Pol II TL single mutant growth fitness profiling across several phenotypes and the single mutants were ordered by hierarchical clustering with Euclidean distance. The lower part of the heatmap shows double mutant deviation scores where a colored block at the interaction of x and y coordinates indicates deviation score of the double mutant.

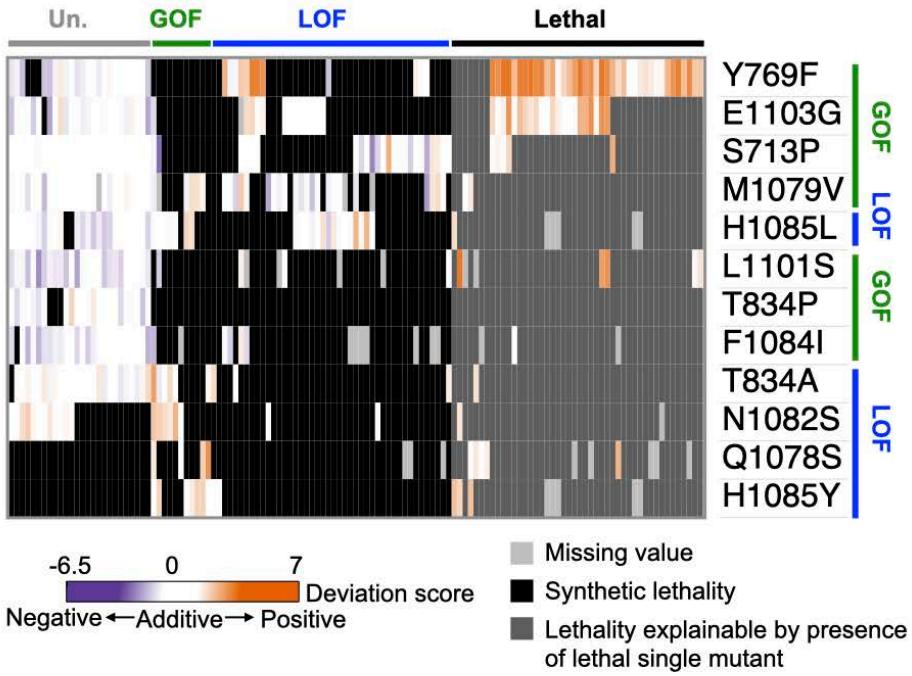

Extended Data Fig.7 Allele-specific interactions. Unique interactions observed between TL substitutions and probe mutants. For each substitution, we analyzed the interquartile range (IQR) of their deviation scores with all probe mutants. Any substitution with deviation score(s) outside of the IQR were extracted and called as unique interaction(s). 127 substitutions with unique interactions with probe mutants were found out of 620 and are shown in the heatmap. The heatmap was hierarchical clustered with Euclidean distance for both rows and columns.

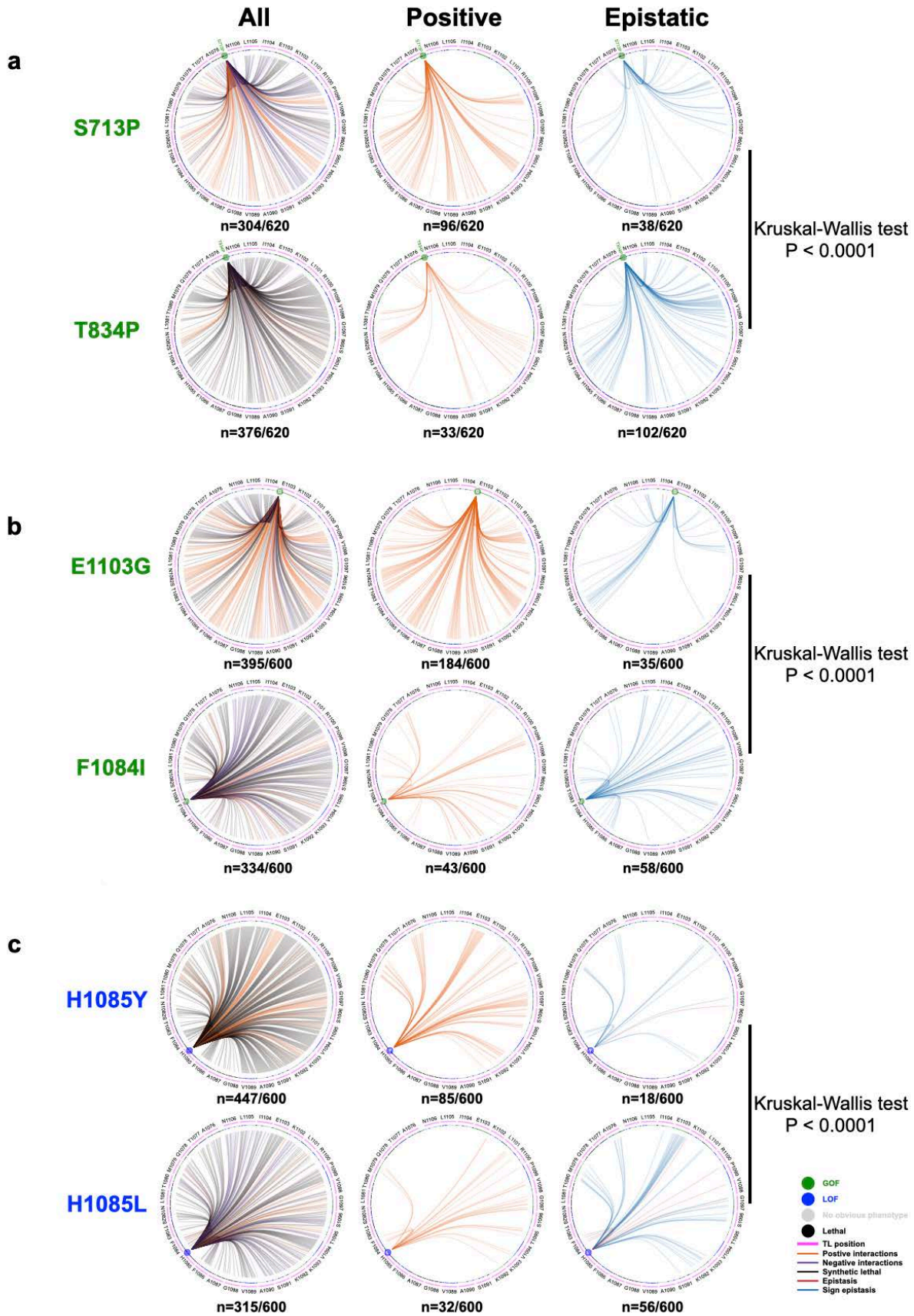
All
Positive
Epistatic
a
S713P
n=304/620
n=96/620
n=38/620
T834P
n=376/620
n=33/620
n=102/620
Kruskal-Wallis test
P < 0.0001
b
E1103G
n=395/600
n=184/600
n=35/600
F1084I
n=334/600
n=43/600
n=58/600
Kruskal-Wallis test
P < 0.0001
c
H1085Y
n=447/600
n=85/600
n=18/600
H1085L
n=315/600
n=32/600
n=56/600
Kruskal-Wallis test
P < 0.0001
GOF
LOF
No obvious phenotype
Lethal
TL position
Postive interactions
Negative interactions
Synthetic lethal
Epistasis
Sign epistasis

1168

Extended Data Fig.8 Interaction networks of selected probe mutants. The TL is shown in circle with WT residues and positions labeled. All 20 substitutions of each TL residue are represented by a magenta arc under each WT residue, with tick marks representing individual substitutions at that position and are colored by mutant class. Comparison of interaction networks between S713P and T834P (**a**), E1103G and F1084I (**b**) and H1085Y and H1085L (**c**) showed the differences are significant ($P < 0.0001$). The comparisons were performed with Kruskal-Wallis test with P-value correction with Dunn's multiple comparisons test (Supplemental Table 7).

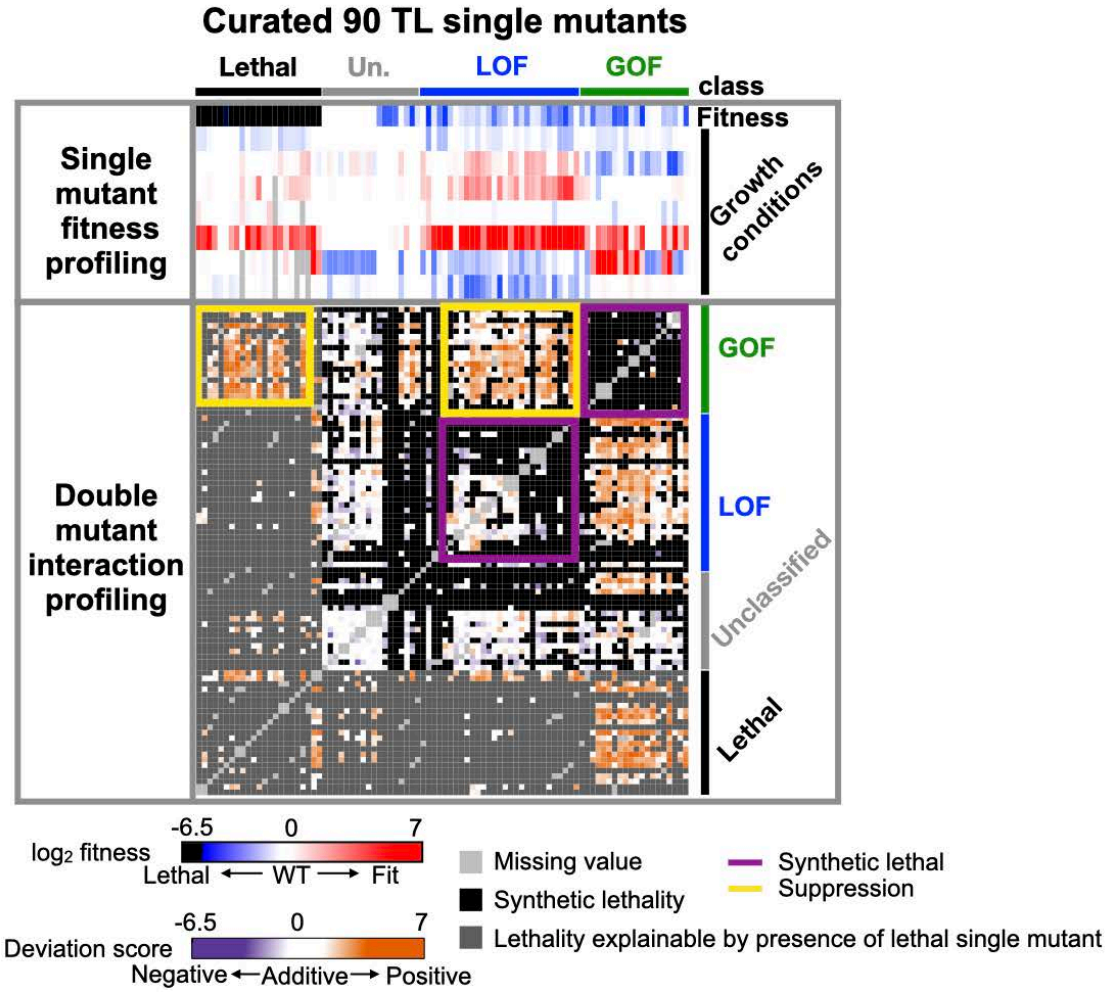

Extended Data Fig.9 The intra-TL functional interaction landscape. The intra-TL functional interaction landscape is shown as a heatmap. Annotations at the top and right indicate the 90 curated single mutants and their predicted phenotypic classes from multiple logistic regression modeling. The upper part of the heatmap shows single mutant growth fitness profiling across multiple phenotypes ordered by groups predicted with logistic regression models. The lower part of the heatmap shows double mutant deviation scores where a colored block at the interaction of x and y coordinates indicates deviation score of the double mutant.

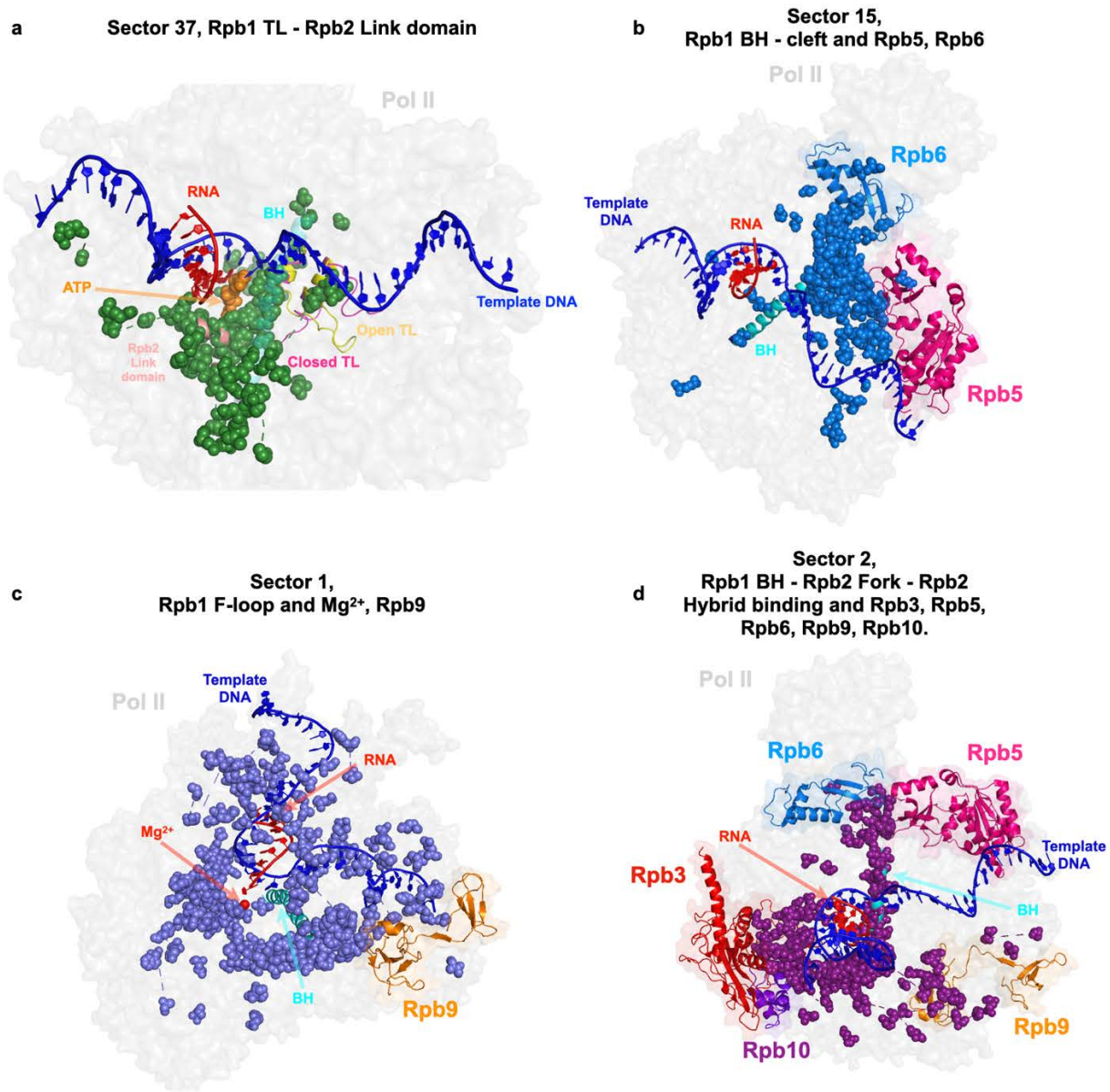

Extended Data Fig.10 Coevolutionary sectors of Pol II active site residues extend to the surface of Pol II, forming connections with other Pol II subunits. a. The coevolutionary sector of Rpb1 TL and Rpb2 link domain residues surrounds the substrate ATP, indicating its potential role in catalysis**.** The sector is mapped on the yeast Pol II structure with TL in open state (PDB: 5C4X) and closed state (PDB: 8U9R). **b**. Residues in sector 15 connect with Rpb5 and Rpb6. **c.** Residues on sector 1 connect with Mg^{2+} and Rpb9. **d.** Residues in sector 2 connect with Rpb5, Rpb6, Rpb3, Rpb9 and Rpb10. These sectors are mapped on the yeast Pol II structure (PDB: 5C4X)[42].

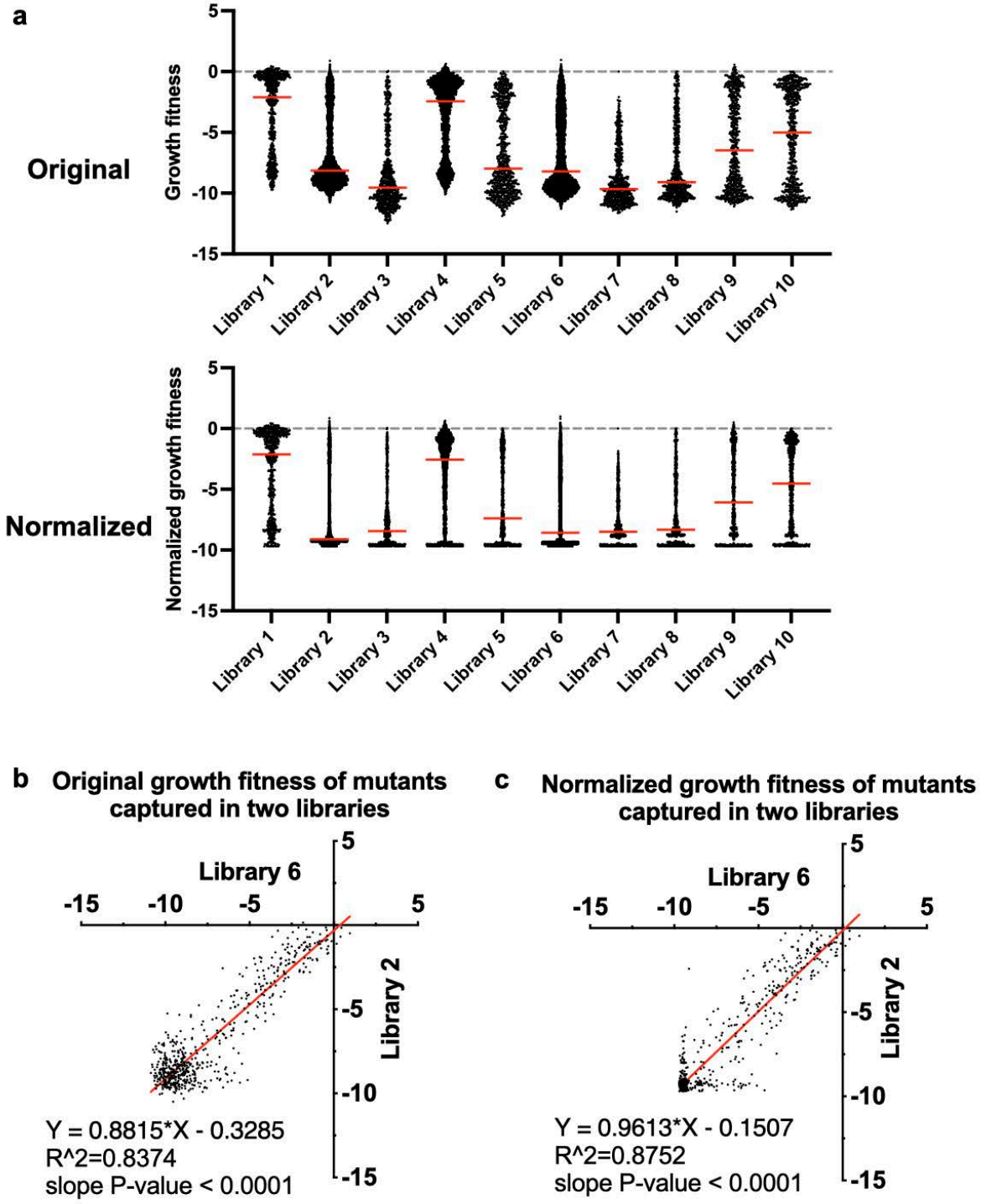

Figure S1. Min-Max normalization uniformed the fitness level of lethal mutants from different libraries without disturbing the median of mutant fitness. a. Library growth fitness distributions before and after normalization. Upper panel: The growth fitness distributions of libraries. The lowest fitness levels (fitness of lethal mutants) are different among libraries. To uniform various lowest fitness levels, we applied Min-Max normalization to minimize library effects on fitness ranges (See **Methods** for details). Lower panel: Libraries fitness distributions after normalization. The lethal mutant fitness levels of libraries were normalized to the same

level while the median fitness for each library was not affected by the normalization. **b-c.** XY-plots showing the original fitness of mutants captured in two different libraries (n=586) (**b**). These mutants present in two libraries showed improved correlation between measurements upon normalization (**c**).

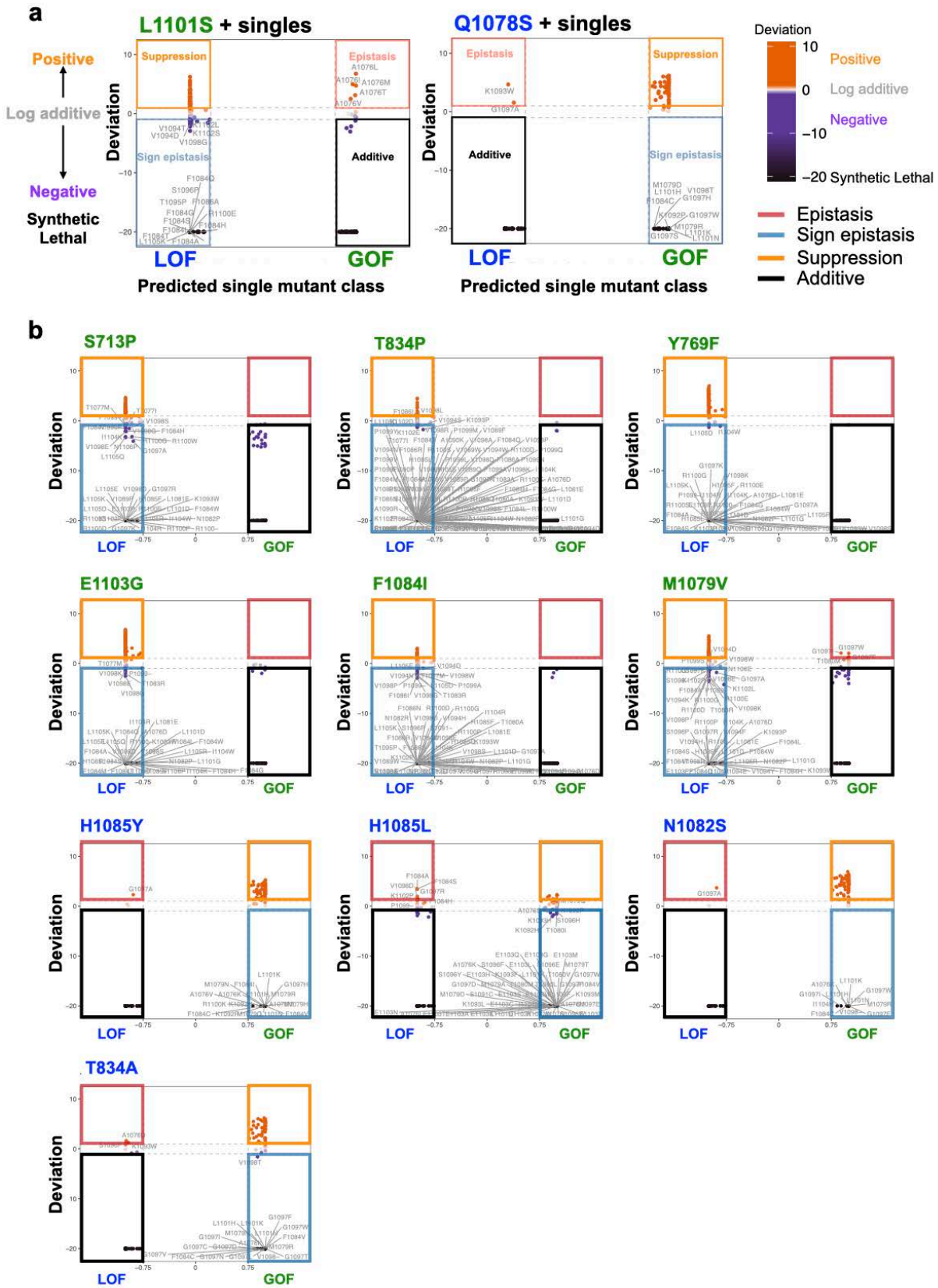
a
L1101S + singles
Q1078S + singles
Positive
Log additive
Negative
Synthetic Lethal
Deviation
Suppression
Epistasis
Sign epistasis
Additive
LOF
GOF
Predicted single mutant class
Deviation
Positive
Log additive
Negative
Synthetic Lethal
Epistasis
Sign epistasis
Suppression
Additive
b
S713P
T834P
Y769F
E1103G
F1084I
M1079V
H1085Y
H1085L
N1082S
T834A

1209

1210 **Figure S2. Identifying TL substitutions that interact with the probe mutants. a.**
1211 Identification of epistasis and suppression within positive interactions, and sign epistasis and
1212 synthetic sickness/lethality within negative interactions in two probe mutants, L1101S and
1213 N1082S. The deviation score of combinations (y-axis) between probe mutants and TL GOF or
1214 LOF single mutants were plotted versus the predicted probability of single mutants being GOF
1215 or LOF (x-axis). **b.** The scatter plots for distinguishing interactions of the other 10 TL probe
1216 mutants.

1217

1218

a **Positive interaction between two viable mutants**

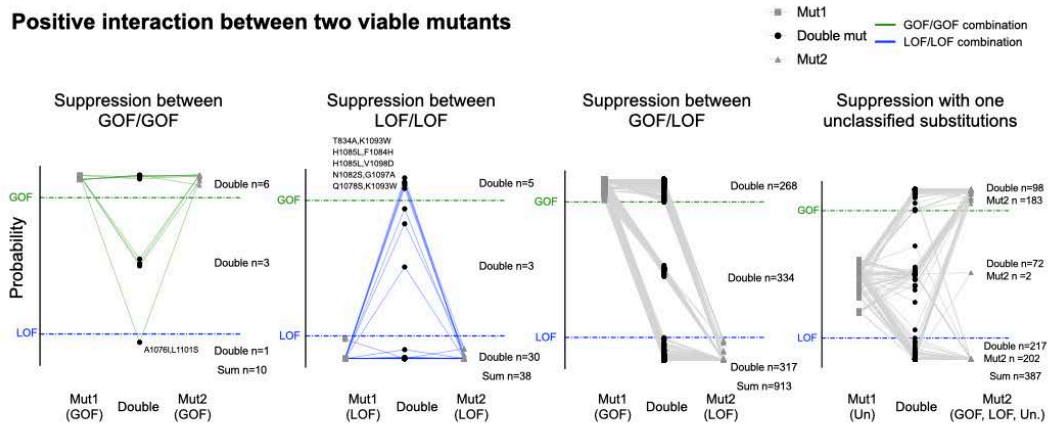

b **Positive interaction (at least one substitution is lethal)**

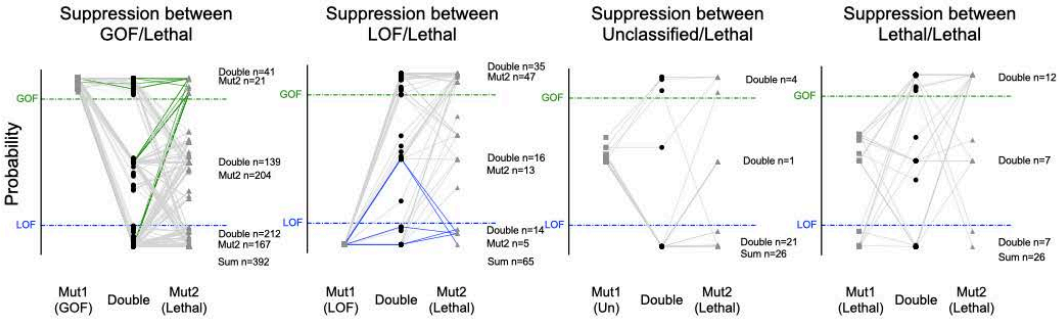

c

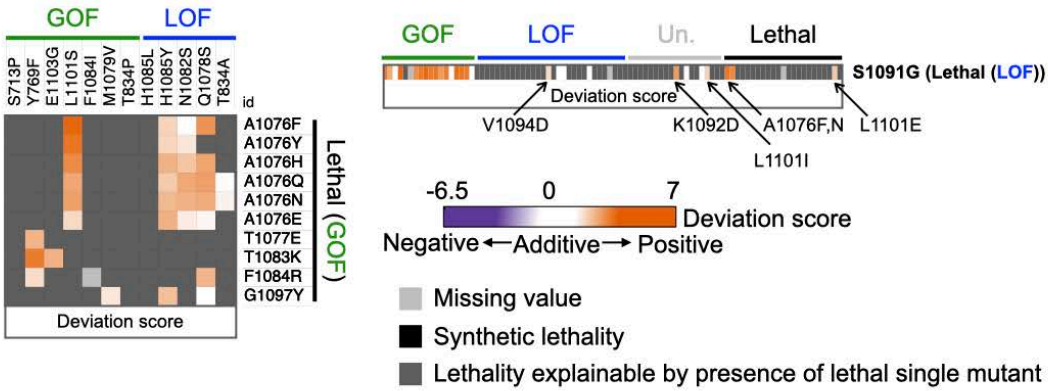

d Ratio of observed strong or weak epistasis

	Strong epistasis (|d| > 2)	Weak epistasis (1< |d| < 2)
Pairwise Intra-TL doubles	0.15	0.06
Target Intra-TL doubles	0.15	0.09
Target Pol II-TL doubles	0.17	0.10
Reported	0.05	0.3

Figure S3. Discrimination of regular epistasis from sign epistasis. a. The phenotypic classes of double mutants consist of two viable single substitutions with positive interactions. Four plots show four kinds of combinations respectively. For each plot, the predicted GOF or LOF probabilities of a double mutant and two constituent single mutants are shown in Y-axis. The double mutant and two constituent single mutants are shown in X-axis in the order of the first constituent mutant (Mut1), the double mutant (Double), the second constituent mutant (Mut2). The double mutant and two constituent mutants are connected with lines for each pair of combinations. The numbers of double mutants belonging to GOF (top), unclassified (middle), or LOF (bottom) are labeled. GOF and LOF probability threshold are labeled with dashed lines. **b.** The phenotypic classes of double mutants consist of one viable and one lethal single substitution, or two lethal single substitutions with positive interactions. The arrangements of plots are similar to **a**. **c.** The heatmaps of lethal GOF substitutions suppressed by GOF targets (left) and lethal LOF substitutions suppressed by LOF targets (right). **d.** The fraction of strong and weak interactions we observed in double mutants compared with the ratio reported in other studies [57,86-89].

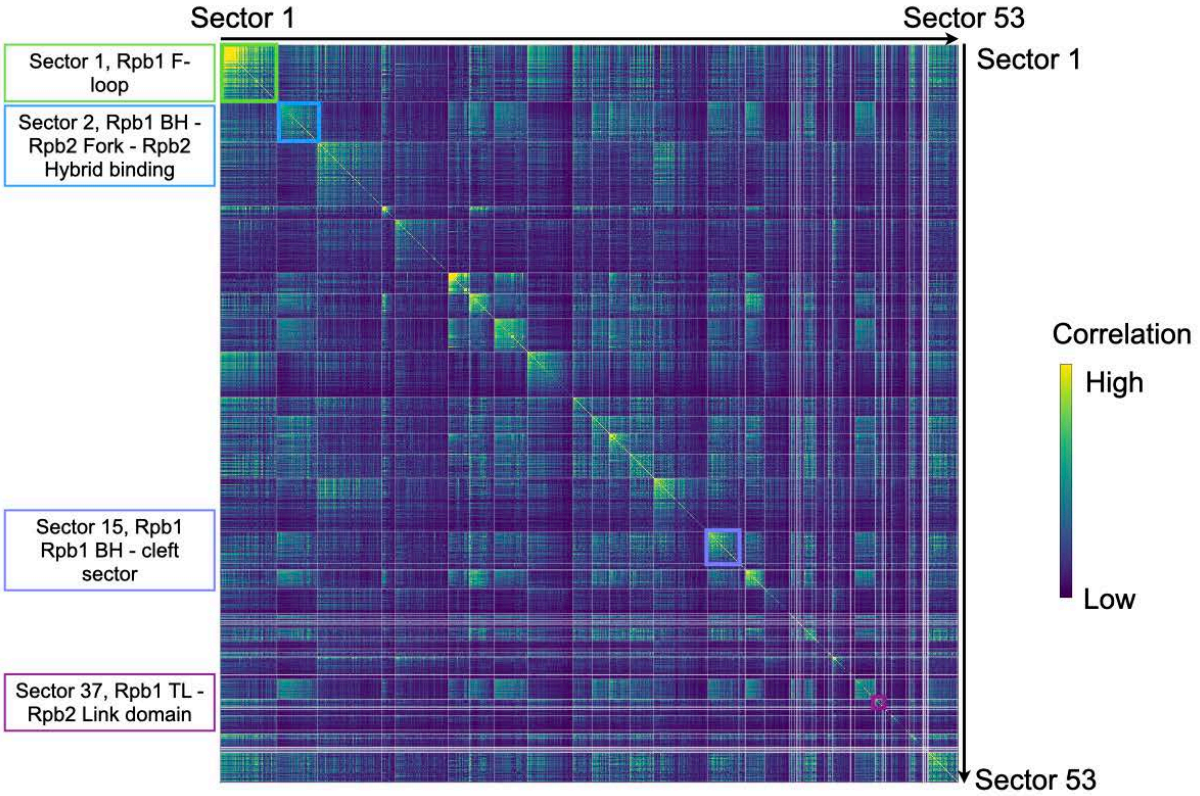

Figure S4. **Rpb1/Rpb2 coevolutionary residue sectors identified by Statistical Coupling Analysis (SCA).** 53 significant and independent sectors are shown in a heatmap with correlation score calculated from the statistical coupling analysis. Four major sectors containing Pol II active site residues are labeled on the left of the heatmap. Statistical coupling analysis was applied to a Multiple Sequence Alignment (MSA) of 283 Rpb1/Rpb2 homologs.

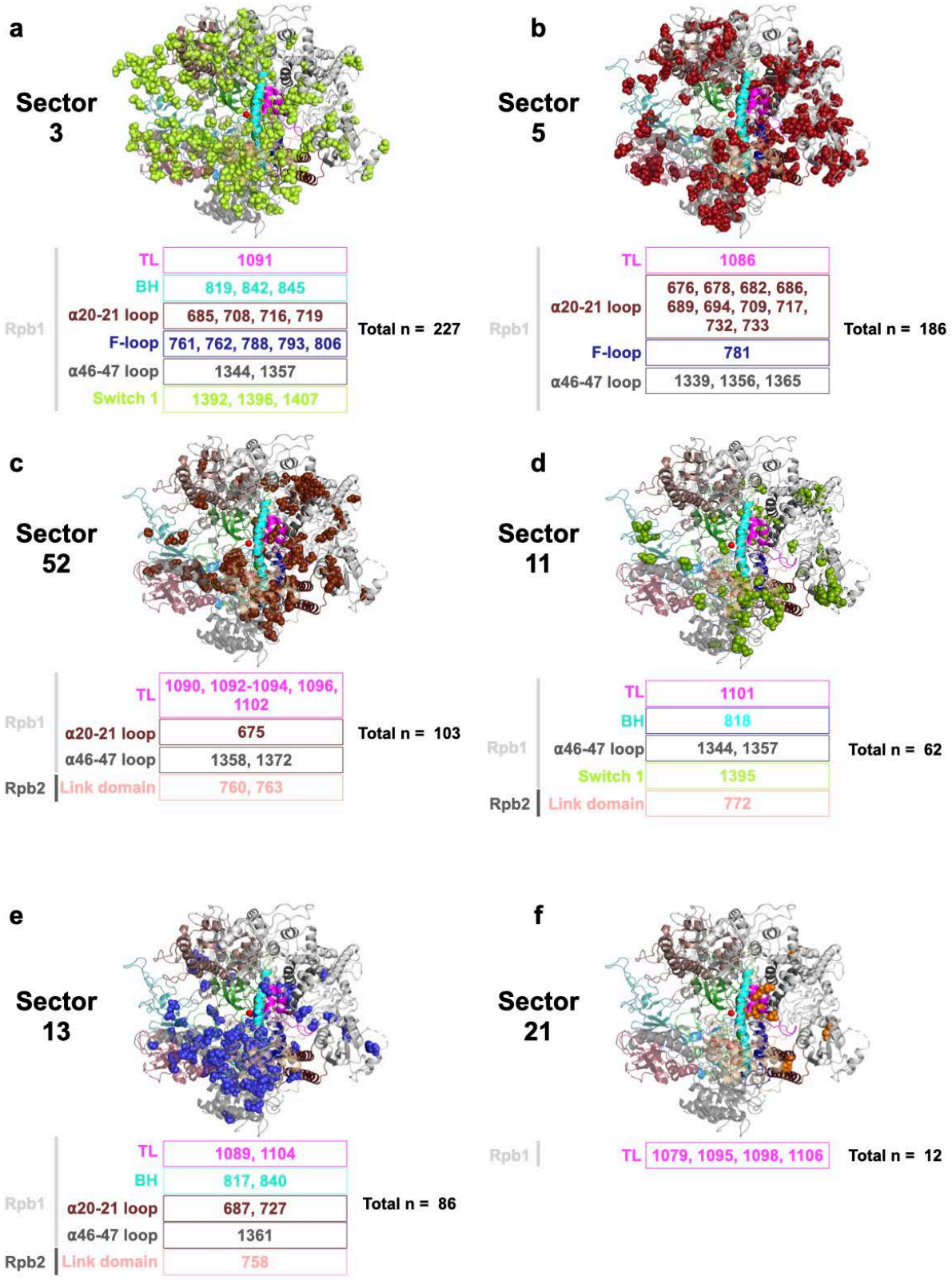
a
Sector 3
Rpb1
TL 1091
BH 819, 842, 845
α20-21 loop 685, 708, 716, 719
F-loop 761, 762, 788, 793, 806
α46-47 loop 1344, 1357
Switch 1 1392, 1396, 1407
Total n = 227
b
Sector 5
Rpb1
TL 1086
α20-21 loop 676, 678, 682, 686, 689, 694, 709, 717, 732, 733
F-loop 781
α46-47 loop 1339, 1356, 1365
Total n = 186
c
Sector 52
Rpb1
TL 1090, 1092-1094, 1096, 1102
α20-21 loop 675
α46-47 loop 1358, 1372
Rpb2
Link domain 760, 763
Total n = 103
d
Sector 11
Rpb1
TL 1101
BH 818
α46-47 loop 1344, 1357
Switch 1 1395
Rpb2
Link domain 772
Total n = 62
e
Sector 13
Rpb1
TL 1089, 1104
BH 817, 840
α20-21 loop 687, 727
α46-47 loop 1361
Rpb2
Link domain 758
Total n = 86
f
Sector 21
Rpb1
TL 1079, 1095, 1098, 1106
Total n = 12

1245

1246 **Figure S5**. **Other coevolutionary networks involving Pol II active site residues.** In addition
1247 to the four major sectors, Pol II active site residues, along with residues in Rpb1/Rpb2, form
1248 additional coevolutionary sectors (**a-f**). Residues within the Pol II active site domains are
1249 labeled. These sectors are mapped on the yeast Pol II Rpb1/Rpb2 structure (PDB: 5C4X)[42].

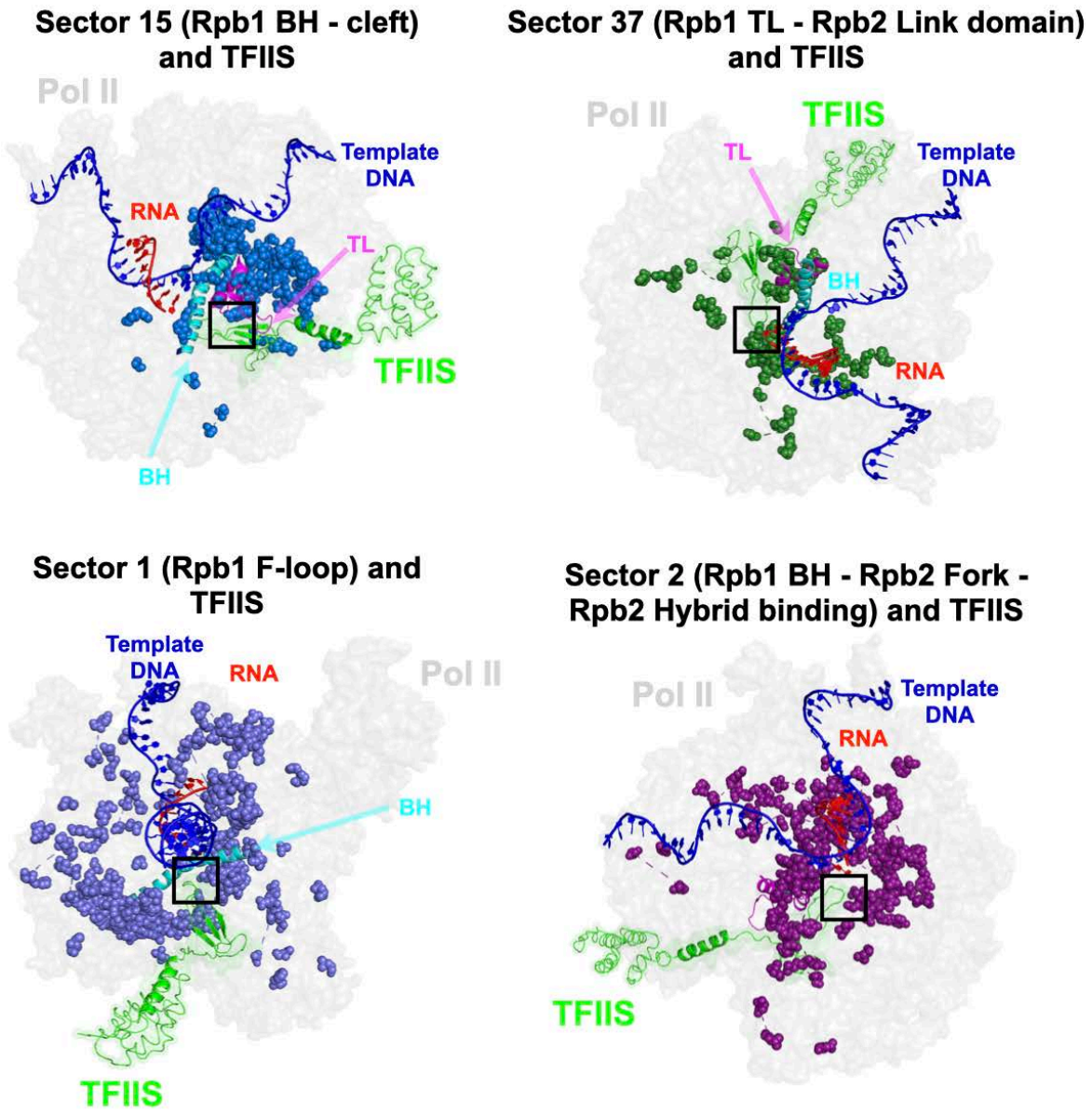

1250

1251 **Figure S6. Coevolutionary residues of four major sectors in Pol II active site interact with**
1252 **TFIIS.** Coevolutionary residues are mapped on the yeast Pol II structure (PDB:5C4X) and
1253 aligned with TFIIS structure (PDB:1Y1V). The interacting residues are highlighted with black box
1254 respectively.

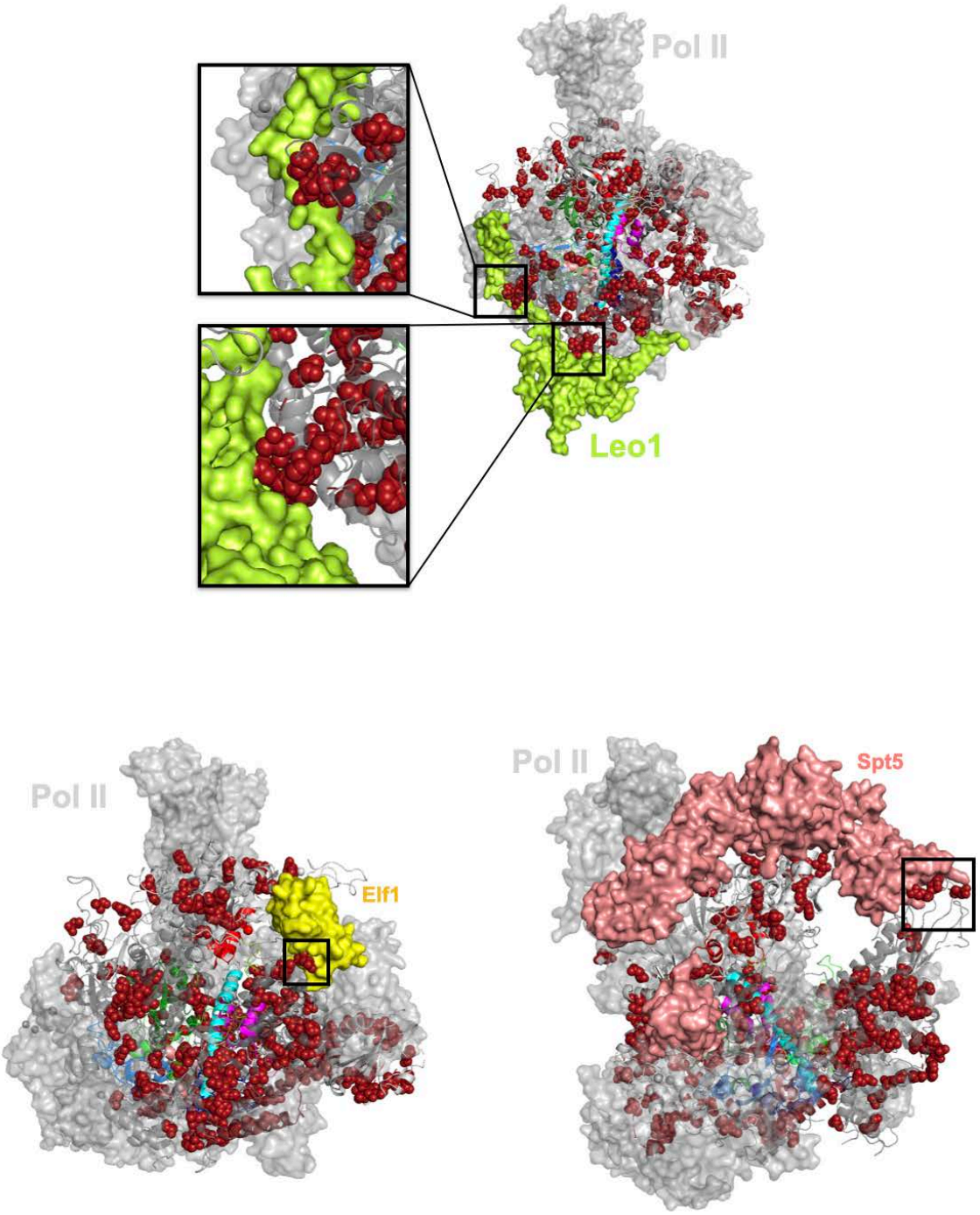

1255

1256 **Figure S7. Residues in Pol II active site coevolutionary sectors extend to the surface of**
1257 **the enzyme and interact with transcription factors.** Coevolutionary residues in sector 5 (**Fig.**
1258 **S16b** in the manuscript) are mapped on the yeast Pol II structure (PDB:5C4X) and aligned with
1259 the structures of transcription factors Leo1, Elf1, and Spt5 (PDB:7xn7). The interacting residues
1260 are highlighted with black box respectively.

1261

1262

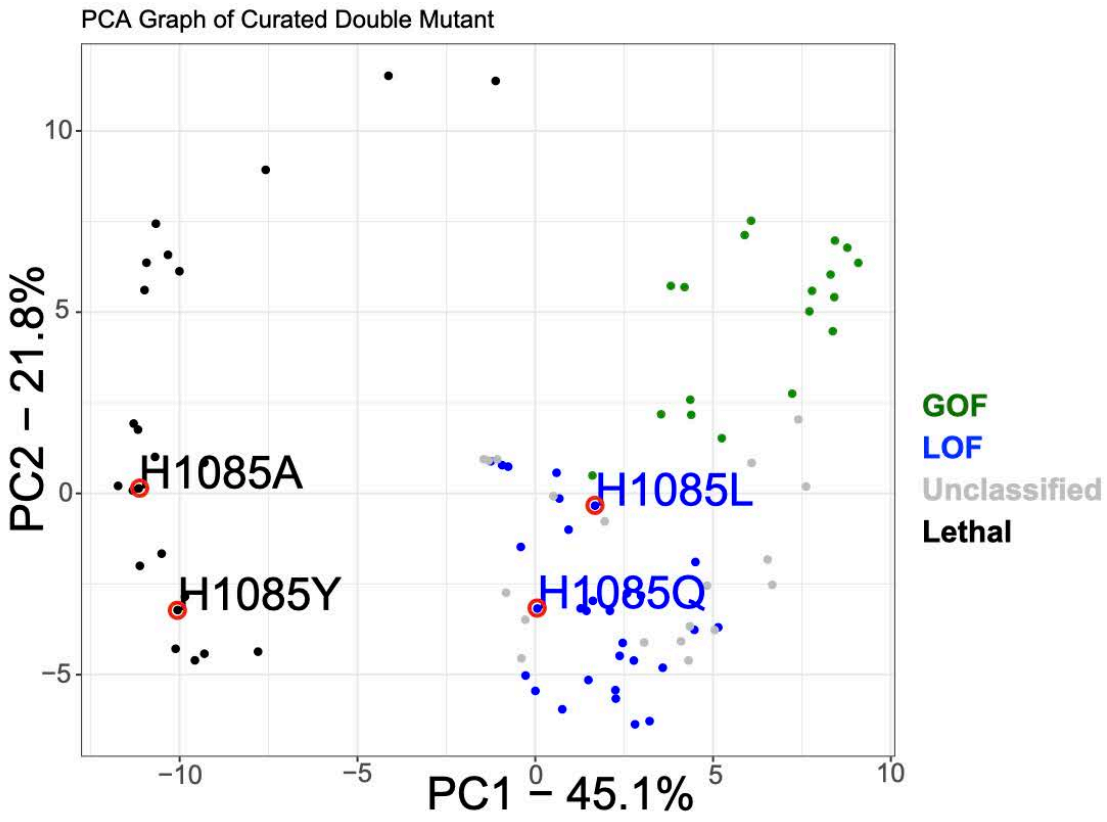

Figure S8. **Four H1085 substitutions are different in some ways. A.** Principal component analysis (PCA) with double mutant deviation scores of all curated TL single mutant substitutions, which are represented with colored dots. GOF mutants are in green, LOF mutants are in blue, unclassified mutants are in grey and lethal mutants are in black. Four H1085 substitutions are labeled and assigned with a red circle to make them visible in the plot.